Quantum Monte Carlo calculations of nuclei with $A \leqslant 7$

B. S. Pudliner* and V. R. Pandharipande[†]

Physics Department, University of Illinois at Urbana-Champaign, 1110 West Green Street, Urbana, Illinois 61801

J. Carlson[‡]

Theoretical Division, Los Alamos National Laboratory, Los Alamos, New Mexico 87545

Steven C. Pieper[§] and R. B. Wiringa[||]

Physics Division, Argonne National Laboratory, Argonne, Illinois 60439

We report quantum Monte Carlo calculations of ground and low-lying excited states for nuclei with $A \leqslant 7$ using a realistic Hamiltonian containing the Argonne v_{18} two-nucleon and Urbana IX three-nucleon potentials. A detailed description of the Green's-function Monte Carlo algorithm for systems with state-dependent potentials is given and a number of tests of its convergence and accuracy are performed. We find that the Hamiltonian being used results in ground states of both ^{6}Li and ^{7}Li that are stable against breakup into subclusters, but somewhat underbound compared to experiment. We also have results for ^{6}He, ^{7}He, and their isobaric analogs. The known excitation spectra of all these nuclei are reproduced reasonably well and we predict a number of excited states in ^{6}He and ^{7}He. We also present spin-polarized one-body and several different two-body density distributions. These are the first microscopic calculations that directly produce nuclear shell structure from realistic interactions that fit NN scattering data. [S0556-2813(97)02810-0]

PACS number(s): 21.10.−k, 21.45.+v, 21.60.Ka, 27.20.+n

I. INTRODUCTION

A major goal in nuclear physics is to understand how nuclear binding, stability, and structure arise from the underlying interactions between individual nucleons. A large amount of empirical information about the nucleon-nucleon scattering problem has been accumulated over time, resulting in ever more sophisticated NN potential models. However, for many years, it has been feasible to calculate exactly only three- and four-body nuclei with realistic NN interactions. Thanks to the ongoing advances in computational resources, particularly the advent of massively parallel computers, it is now possible to apply sophisticated quantum Monte Carlo methods to the study of light p-shell nuclei, which have a far richer spectrum to investigate.

The p shell has long been a testing ground for shell model methods [1]. Shell-model studies of $A = 4-7$ nuclei have recently progressed to the stage of large-basis, ''no-core'' calculations using G matrices derived from the latest NN-interaction models [2]. Alternatively, there have been extensive studies of these light nuclei with cluster-cluster models, using combinations of NN and αN potentials [3]. Our goal here is to calculate properties, in particular ground-state energies, of the light p-shell nuclei directly from bare NN and NNN interactions, without any intermediate effective interaction.

Recently we reported [4] results for the ground states of ^{6}He, ^{6}Li, and ^{6}Be, and the first two excited states in ^{6}Li, calculated with the Green's-function Monte Carlo (GFMC) method for a Hamiltonian containing the Argonne v_{18} NN and Urbana IX NNN potentials. Here we present improved and extended calculations for the $A = 6$ nuclei and the first detailed studies of ^{7}He, ^{7}Li, ^{7}Be, and ^{7}B, including all the observed low-lying excitations. In this work, it is possible to see the full splendor of the nuclear shell structure emanating directly from a microscopic interaction that fits NN scattering data.

The Argonne v_{18} model [5] is one of a class of new, highly accurate NN potentials that fit both pp and np scattering data up to 350 MeV with a χ^2/datum near 1. This necessarily involves the introduction of charge-independence breaking in the strong force; a complete electromagnetic interaction is also included as an integral part of the model. This makes the model useful for studying charge dependence and charge-symmetry breaking in nuclei. The NN potential is supplemented by a three-nucleon interaction from the Urbana series of NNN potentials [6], including both long-range two-pion exchange and a short-range phenomenological component. The Urbana model IX is adjusted to reproduce the binding energy of ^{3}H and give a reasonable saturation density in nuclear matter when used with Argonne v_{18}. Details of the Hamiltonian are given in Sec. II.

The first step in our calculation is the construction of suitable trial functions. Variational wave functions based on products of correlated operators have been used successfully for ^{3}H and ^{4}He, giving binding energies about 2% above exact Faddeev, hyperspherical harmonic, or GFMC solutions [7]. We generalize this type of trial function for $A = 6,7$ nuclei, adding p-wave orbitals and using LS coupling to produce all possible $(J^\pi; T)$ quantum states. Parameters in the

---

*Present address: Scientific Computing Applications Division, Lawrence Livermore National Laboratory, Livermore, CA 94551; electronic address: pudliner@llnl.gov

[†]Electronic address: vijay@rsm1.physics.uiuc.edu

[‡]Electronic address: carlson@qmc.lanl.gov

[§]Electronic address: spieper@anl.gov

[||]Electronic address: wiringa@theory.phy.anl.gov

trial functions are adjusted to minimize the energy expectation value, evaluated with Monte Carlo integration, subject to the constraint that rms radii are close to the experimental values for ^{6}Li and ^{7}Li. Unfortunately, the best trial functions we have been able to build do not give p-shell nuclei stable against breakup into subclusters. Nevertheless, these trial functions provide a good starting point for the GFMC calculation. The variational wave functions and a brief description of the variational Monte Carlo (VMC) calculations are given in Sec. III.

The GFMC method projects out the exact lowest energy state, Ψ_0, for a given set of quantum numbers, from a suitable trial function, Ψ_T, using $\Psi_0 = \lim_{\tau\to\infty} \exp[-(H-E_0)\tau]\Psi_T$. The method has been used with great success in a variety of condensed-matter problems, and in s-shell nuclei with realistic interactions [8]. Our first calculations for p-shell nuclei [4] were made with a short-time approximation for the propagation in imaginary time, carried out to $\tau = 0.06$ MeV^{-1} and extrapolated to $\tau = \infty$. In the present work we have improved the algorithm by adopting an exact two-body propagator which allows bigger time steps, saving significantly on the computational cost. We also have started our calculations with better trial functions, which allows more reliable results to be obtained from GFMC propagations that are limited to small τ. A detailed discussion of the method as applied to realistic nuclear forces is given in Sec. IV.

The VMC and GFMC calculations for p-shell nuclei are very computer intensive, and would not have been possible without the recent advances in computational power due to the advent of massively parallel machines. Section V describes the implementation of the GFMC algorithm in a parallel environment, including issues of communication between processors and load balancing. We have also performed a number of tests of the GFMC method, including comparisons to other exact calculations for s-shell nuclei, studies of extrapolation in τ, and sensitivity to the quality of the input trial function. These tests are described in Sec. VI.

Results of our GFMC calculations are presented in Sec. VII. We have obtained energies for five states of unique $(J^\pi;T)$ in the $A=6$ nuclei, and another five states in $A=7$ nuclei, not counting isobaric analog states. In general we find the nuclei are slightly underbound with the present Hamiltonian, but ^{6}Li (^{7}Li) is stable against breakup into $\alpha+d$ ($\alpha+t$). The low-lying excited states are correctly ordered with reasonable excitation energies. The VMC energies are found to lie ~ 3 (4.5) MeV above the GFMC results in $A=6$ (7) nuclei, but with very similar excitation energies. We have also used the VMC wave functions to perform small-basis diagonalizations of states with the same quantum numbers but different symmetries. These calculations optimize the admixtures of different-symmetry contributions to the ground state, and also provide estimates for higher-lying excited states with the same $(J^\pi;T)$ quantum numbers. We verify that these states, not all of which have been observed, do indeed lie at moderately higher excitations. The VMC spectra are also discussed in Sec. VII.

One- and two-body density distributions from both VMC and GFMC calculations are presented in Sec. VIII. These include the densities of spin-up/down nucleons in polarized ^{6}Li and ^{7}Li. In general, the GFMC densities are slightly more peaked than the input VMC densities, but overall they are very similar. Unfortunately, both VMC and GFMC calculations are not very sensitive to the very long-range properties of the wave functions. Therefore it is not yet possible to accurately calculate the quadrupole moments and asymptotic D/S ratios with these methods. Finally, we present our conclusions in Sec. IX.

II. HAMILTONIAN

Our Hamiltonian includes a nonrelativistic one-body kinetic energy, the Argonne v_{18} two-nucleon potential [5] and the Urbana IX three-nucleon potential [4],

$$H = \sum_i K_i + \sum_{i<j} v_{ij} + \sum_{i<j<k} V_{ijk}. \qquad (2.1)$$

The kinetic energy operator has charge-independent (CI) and charge-symmetry-breaking (CSB) components, the latter due to the difference in proton and neutron masses,

$$K_i = K_i^{CI} + K_i^{CSB} \equiv -\frac{\hbar^2}{4}\left(\frac{1}{m_p}+\frac{1}{m_n}\right)\nabla_i^2$$
$$-\frac{\hbar^2}{4}\left(\frac{1}{m_p}-\frac{1}{m_n}\right)\tau_{zi}\nabla_i^2. \qquad (2.2)$$

The Argonne v_{18} potential can be written as a sum of electromagnetic and one-pion-exchange terms and a shorter-range phenomenological part,

$$v_{ij} = v_{ij}^\gamma + v_{ij}^\pi + v_{ij}^R. \qquad (2.3)$$

The electromagnetic terms include one- and two-photon-exchange Coulomb interaction, vacuum polarization, Darwin-Foldy, and magnetic moment terms, with appropriate proton and neutron form factors:

$$v^\gamma(pp) = V_{C1}(pp) + V_{C2} + V_{VP} + V_{DF} + V_{MM}(pp), \qquad (2.4)$$

$$v^\gamma(np) = V_{C1}(np) + V_{MM}(np), \qquad (2.5)$$

$$v^\gamma(nn) = V_{MM}(nn). \qquad (2.6)$$

The V_{MM} contain spin-spin, tensor, and spin-orbit components. Detailed expressions for these terms, including the form factors, are given in Ref. [5]. These terms should be included in calculations aiming for better than 99% accuracy. For example, the contribution of $v^\gamma(np)$ to the binding energy of the deuteron is ~ 0.02 MeV, i.e., 1% of the total.

The one-pion-exchange part of the potential includes the charge-dependent (CD) terms due to the difference in neutral and charged pion masses. It can be written in an operator format as

$$v_{ij}^\pi = f^2\left(\frac{m}{m_s}\right)^2 \frac{1}{3}mc^2[X_{ij}\tau_i\cdot\tau_j + \widetilde{X}_{ij}T_{ij}], \qquad (2.7)$$

where $T_{ij} = 3\tau_{zi}\tau_{zj} - \tau_i\cdot\tau_j$ is the isotensor operator and

$$X_{ij} = \frac{1}{3}(X_{ij}^0 + 2X_{ij}^\pm), \qquad (2.8)$$

$$\widetilde{X}_{ij} = \tfrac{1}{3}(X_{ij}^0 - X_{ij}^\pm), \qquad (2.9)$$

$$X_{ij}^m = [Y(mr)\sigma_i \cdot \sigma_j + T(mr)S_{ij}]. \qquad (2.10)$$

Here $Y(mr)$ and $T(mr)$ are the normal Yukawa and tensor functions with a cutoff specified in Ref. [5], and $X^{\pm,0}$ are calculated with $m = m_{\pi^\pm}$ and m_{π^0}.

The one-pion-exchange and the remaining phenomenological part of the potential can be written as a sum of 18 operators,

$$v_{ij}^\pi + v_{ij}^R = \sum_{p=1,18} v_p(r_{ij})O_{ij}^p. \qquad (2.11)$$

The first 14 are charge independent,

$$O_{ij}^{p=1,14} = [1,(\sigma_i \cdot \sigma_j),S_{ij},(\mathbf{L\cdot S}),\mathbf{L}^2,\mathbf{L}^2(\sigma_i \cdot \sigma_j),(\mathbf{L\cdot S})^2]$$
$$\otimes [1,(\tau_i \cdot \tau_j)], \qquad (2.12)$$

and the last four,

$$O_{ij}^{p=15,18} = [1,(\sigma_i \cdot \sigma_j),S_{ij}] \otimes T_{ij},(\tau_{zi} + \tau_{zj}), \qquad (2.13)$$

break charge independence. We will refer to the potential from the $p = 15 - 17$ terms as v^{CD} and from the $p = 18$ term as v^{CSB}. We note that in the context of isospin symmetry the CI, CSB, and CD terms are respectively isoscalar, isovector, and isotensor.

The potential was fit directly to the Nijmegen NN scattering data base [9,10] containing 1787 pp and 2514 np data in the range $0 - 350$ MeV, with a χ^2 per datum of 1.09. It was also fit to the nn scattering length measured in $d(\pi^-,\gamma)nn$ experiments and the deuteron binding energy. There could, in principle, be more charge-independence-breaking (CIB) terms such as $\mathbf{L\cdot S}T_{ij}$ or $S_{ij}(\tau_{zi} + \tau_{zj})$ but the scattering data are not sufficiently precise to identify them at present.

The Urbana series of three-nucleon potentials is written as a sum of two-pion-exchange and shorter-range phenomenological terms,

$$V_{ijk} = V_{ijk}^{2\pi} + V_{ijk}^R. \qquad (2.14)$$

The two-pion-exchange term can be expressed simply as

$$V_{ijk}^{2\pi} = \sum_{\text{cyclic}} A_{2\pi}\{X_{ij}^\pi,X_{jk}^\pi\}\{\tau_i \cdot \tau_j,\tau_j \cdot \tau_k\}$$
$$+ C_{2\pi}[X_{ij}^\pi,X_{jk}^\pi][\tau_i \cdot \tau_j,\tau_j \cdot \tau_k], \qquad (2.15)$$

where X_{ij}^π is constructed with an average pion mass, $m_\pi = \tfrac{1}{3}m_{\pi^0} + \tfrac{2}{3}m_{\pi^\pm}$. The anticommutator and commutator terms are denoted by V_{ijk}^A and V_{ijk}^C, respectively, and for the Urbana models $C_{2\pi} = \tfrac{1}{4}A_{2\pi}$, as in the original Fujita-Miyazawa model [11]. The shorter-range phenomenological term is given by

$$V_{ijk}^R = \sum_{\text{cyclic}} U_0 T^2(m_\pi r_{ij})T^2(m_\pi r_{jk}). \qquad (2.16)$$

The parameters for model IX are $A_{2\pi} = -0.0293$ MeV and $U_0 = 0.0048$ MeV. They have been determined by fitting the density of nuclear matter and the binding energy of ^{3}H in conjunction with the Argonne v_{18} interaction. These values are only slightly different from the model VIII values, $A_{2\pi} = -0.028$ MeV and $U_0 = 0.005$ MeV, that were adjusted for use with the older Argonne v_{14} interaction. In principle, the V_{ijk}^R can have other terms [12], however we need additional data to obtain their strengths; presumably a part of it is due to relativistic effects [13–15].

Direct GFMC calculations with the full interaction (in particular spin-dependent terms which involve the square of the momentum operator) have very large statistical errors, for reasons that will be discussed in Sec. IV. Also the CIB terms in H are fairly weak and therefore can be treated conveniently as a first-order perturbation. Further, using a wave function of good isospin significantly reduces the cost of the calculations. Hence we construct the GFMC propagator with a simpler isoscalar Hamiltonian,

$$H' = \sum_i K_i^{\text{CI}} + \sum_{i<j} v_{ij}' + \sum_{i<j<k} V_{ijk}', \qquad (2.17)$$

where v_{ij}' is defined as

$$v_{ij}' = \sum_{p=1,8} v_p'(r_{ij})O_{ij}^p + v_C'(r_{ij}). \qquad (2.18)$$

The interaction v_{ij}' has only eight operator terms, with operators $[1,(\sigma_i \cdot \sigma_j),S_{ij},(\mathbf{L\cdot S})] \otimes [1,(\tau_i \cdot \tau_j)]$, chosen such that it equals the isoscalar part of the full interaction in all S and P waves as well as in the $^3D_1$ wave and its coupling to the $^3S_1$. The strong interaction terms are related to the full v_{ij} by

$$v_1' = v_1 + \tfrac{5}{4}v_9 + \tfrac{3}{4}v_{10} + \tfrac{3}{4}v_{11} + \tfrac{9}{4}v_{12} + \tfrac{3}{4}v_{13} + \tfrac{3}{4}v_{14},$$

$$v_2' = v_2 + \tfrac{1}{4}v_9 + \tfrac{3}{4}v_{10} + \tfrac{3}{4}v_{11} - \tfrac{3}{4}v_{12} + \tfrac{1}{4}v_{13} + \tfrac{1}{4}v_{14},$$

$$v_3' = v_3 + \tfrac{1}{4}v_9 + \tfrac{3}{4}v_{10} + \tfrac{3}{4}v_{11} - \tfrac{3}{4}v_{12} + \tfrac{1}{4}v_{13} + \tfrac{1}{4}v_{14},$$

$$v_4' = v_4 + \tfrac{1}{4}v_9 - \tfrac{1}{4}v_{10} - \tfrac{1}{4}v_{11} + \tfrac{5}{4}v_{12} + \tfrac{1}{12}v_{13} + \tfrac{1}{12}v_{14},$$

$$v_5' = v_5 - \tfrac{5}{16}v_{13} - \tfrac{5}{16}v_{14},$$

$$v_6' = v_6 - \tfrac{5}{48}v_{13} - \tfrac{5}{48}v_{14},$$

$$v_7' = v_7 - \tfrac{1}{2}v_9 + \tfrac{3}{2}v_{10} - \tfrac{1}{2}v_{11} + \tfrac{3}{2}v_{12} - \tfrac{9}{8}v_{13} + \tfrac{15}{8}v_{14},$$

$$v_8' = v_8 + \tfrac{1}{2}v_9 - \tfrac{3}{2}v_{10} + \tfrac{1}{2}v_{11} - \tfrac{3}{2}v_{12} + \tfrac{5}{8}v_{13} - \tfrac{19}{8}v_{14}. \qquad (2.19)$$

The isoscalar part of $V_{C1}(pp)$ is also included in H'. We derive it by writing the projector for a pair of protons in terms of isoscalar, isovector, and isotensor operators:

$$\tfrac{1}{4}(1 + \tau_{zi})(1 + \tau_{zj}) = \tfrac{1}{4}(1 + \tfrac{1}{3}\tau_i \cdot \tau_j + \tau_{zi} + \tau_{zj} + \tfrac{1}{3}T_{ij}), \qquad (2.20)$$

$$v_C'(r_{ij}) = [\alpha_C(A,Z,T) + \tfrac{1}{12}\tau_i \cdot \tau_j]V_{C1}(pp), \qquad (2.21)$$

$$\alpha_C(A,Z,T) = \frac{1}{A(A-1)}[Z(Z-1) + \tfrac{1}{4}A - \tfrac{1}{3}T(T+1)]. \qquad (2.22)$$

The sum over all pairs of $\alpha_C(A,Z,T) + \frac{1}{12}\tau_i \cdot \tau_j$ is just the number of pp pairs in the given nucleus.

The v'_{ij} is a little more attractive than v_{ij}; for example, ^{4}He is overbound by ~ 2 MeV with v'_{ij}. The expectation value of the difference $\langle v_{ij} - v'_{ij} \rangle$ scales like $\langle V_{ijk} \rangle$, presumably because three-body and higher-order clusters give important contributions to it. Note that in ^{3}H and ^{4}He the two-body cluster gives zero contribution to $\langle v_{ij} - v'_{ij} \rangle$ since they are identical in low partial waves. We compensate for this tendency towards overbinding by using a V'_{ijk} in which the repulsive U_0 term of Eq. (2.16) has been increased by $\sim 30\%$ in the H'. This ensures $\langle H' \rangle \approx \langle H \rangle$ so that the GFMC propagation does not produce excessively large densities due to overbinding. The contribution of $(H - H')$ is calculated perturbatively.

III. VARIATIONAL MONTE CARLO

The variational method can be used to obtain approximate solutions to the many-body Schrödinger equation, $H\Psi = E\Psi$, for a wide range of nuclear systems, including few-body nuclei, light closed shell nuclei, nuclear matter, and neutron stars [16]. A suitably parametrized wave function, Ψ_V, is used to calculate an upper bound to the exact ground-state energy,

$$E_V = \frac{\langle \Psi_V | H | \Psi_V \rangle}{\langle \Psi_V | \Psi_V \rangle} \geq E_0. \qquad (3.1)$$

The parameters in Ψ_V are varied to minimize E_V, and the lowest value is taken as the approximate ground-state energy.

Upper bounds to excited states are also obtainable, either from standard VMC calculations if they have different quantum numbers from the ground state, or from small-basis diagonalizations if they have the same quantum numbers. The corresponding Ψ_V can then be used to calculate other properties, such as particle density or electromagnetic moments, or it can be used as the starting point for a Green's-function Monte Carlo calculation. In this section we first describe our *ansatz* for Ψ_V for the light p-shell nuclei and then briefly review how the expectation value, Eq. (3.1), is evaluated and the parameters of Ψ_V are fixed.

A. Wave function

Our best variational wave function for the nuclei studied here has the form [7]

$$|\Psi_V\rangle = \left[1 + \sum_{i<j<k} (U_{ijk} + U_{ijk}^{TNI}) + \sum_{i<j} U_{ij}^{LS} \right] |\Psi_P\rangle, \qquad (3.2)$$

where the pair wave function, Ψ_P, is given by

$$|\Psi_P\rangle = \left[\mathcal{S}\prod_{i<j} (1 + U_{ij}) \right] |\Psi_J\rangle. \qquad (3.3)$$

The U_{ij}, U_{ij}^{LS}, U_{ijk}, and U_{ijk}^{TNI} are noncommuting two- and three-nucleon correlation operators, and the $\mathcal{S}$ is a symmetrization operator. The form of the totally antisymmetric Ja-

TABLE I. Values of shape parameters used in generation of trial functions. All units in fm. Notation is same as Ref. [17].

a_0	0.35	c_0	1.1	R_0	0.75
a_1	0.4	c_1	3.0	R_1	2.8
a_t	0.4	d	2.0	R_t	3.7
a_b	0.24			R_b	0.4

strow wave function, Ψ_J, depends on the nuclear state under investigation. For the s-shell nuclei we use the simple form

$$|\Psi_J\rangle = \left[\prod_{i<j<k} f_{ijk}^c \right]\left[\prod_{i<j} f_c(r_{ij}) \right] |\Phi_A(JMTT_3)\rangle. \qquad (3.4)$$

Here $f_c(r_{ij})$ and f_{ijk}^c are central two- and three-body correlation functions and

$$|\Phi_3(\tfrac{1}{2}\tfrac{1}{2}\tfrac{1}{2}\tfrac{1}{2})\rangle = \mathcal{A}|p\uparrow p\downarrow n\uparrow\rangle, \qquad (3.5)$$

$$|\Phi_4(0000)\rangle = \mathcal{A}|p\uparrow p\downarrow n\uparrow n\downarrow\rangle. \qquad (3.6)$$

The two-body correlation operator U_{ij} is a sum of spin, isospin, and tensor terms:

$$U_{ij} = \sum_{p=2,6} \left[\prod_{k\neq i,j} f_{ijk}^p(\mathbf{r}_{ik},\mathbf{r}_{jk}) \right] u_p(r_{ij}) O_{ij}^p, \qquad (3.7)$$

while the two-body spin-orbit correlation operator is given by

$$U_{ij}^{LS} = \sum_{p=7,8} u_p(r_{ij}) O_{ij}^p, \qquad (3.8)$$

with

$$O_{ij}^{p=1,8} = [1, \sigma_i \cdot \sigma_j, S_{ij}, (\mathbf{L}\cdot\mathbf{S})_{ij}] \otimes [1, \tau_i \cdot \tau_j]. \qquad (3.9)$$

The U_{ij} and U_{ij}^{LS} correlations are induced by the two-nucleon interaction. The equations used to generate the functions $f_c(r_{ij})$ and $u_p(r_{ij})$ are given in Ref. [17]; they contain a number of variational parameters to be determined by minimizing the energy. The shape parameters listed in Table I seem to have negligible A dependence. Their values are determined by minimizing the ^{3}H energy, and are then used for all subsequent $A \geq 4$ calculations. There are also a number of parameters that describe the long-range behavior of the correlation functions which do vary with A, as well as with the Hamiltonian. Our best values for these parameters are given in Table II.

The f_{ijk}^c, f_{ijk}^p, and U_{ijk} are three-nucleon correlations induced by v_{ij}. The first two have an operator-independent form:

$$f_{ijk}^c = 1 + q_1^c(\mathbf{r}_{ij}\cdot\mathbf{r}_{ik})(\mathbf{r}_{ji}\cdot\mathbf{r}_{jk})(\mathbf{r}_{ki}\cdot\mathbf{r}_{kj})\exp(-q_2^c R_{ijk}), \qquad (3.10)$$

$$f_{ijk}^p = 1 - q_1^p(1 - \hat{\mathbf{r}}_{ik}\cdot\hat{\mathbf{r}}_{jk})\exp(-q_2^p R_{ijk}), \qquad (3.11)$$

where $R_{ijk} = r_{ij} + r_{ik} + r_{jk}$. The U_{ijk} involve additional spin-isospin operators and are somewhat more complicated; they are discussed in Ref. [7]. The U_{ijk}^{TNI} are three-body correla-

TABLE II. Values of asymptotic parameters used in generation of trial functions. Notation is same as Ref. [17].

	^{3}H	$A \geqslant 4$
$E_{0,0}$ (MeV)	3.2	17.0
$E_{0,1}$ (MeV)	6.0	16.0
$E_{1,0}$ (MeV)	13.0	23.5
$E_{1,1}$ (MeV)	6.4	16.5
$h_{0,0}$	0.85	1.04
$h_{0,1}$	1.70	1.71
$h_{1,0}$	1.74	1.54
$h_{1,1}$	1.72	1.68
η_0	0.026	0.035
η_1	-0.007	-0.015
ζ_1	0.0003	0.0003
α_t	0.92	0.86

tions induced by the three-nucleon interaction, which we take in the form suggested by perturbation theory:

$$U_{ijk}^{\text{TNI}} = \sum_x \epsilon_x V_{ijk}^x(\widetilde{r}_{ij}, \widetilde{r}_{jk}, \widetilde{r}_{ki}), \qquad (3.12)$$

with $\widetilde{r} = yr$, y a scaling parameter, and ϵ_x a strength parameter. Here $x = A$, C, and R refers to the different parts of the *NNN* potential. With the present Hamiltonian we use the three-body parameters given in Table III for all nuclei studied here.

The relative importance and cost of computing different elements of the full variational wave function Ψ_V are shown in Table IV for the case of ^{6}Li. The pair wave function Ψ_P is the least expensive to compute, but gives a rather poor energy. The successive addition of U_{ijk}^{TNI}, U_{ij}^{LS}, and U_{ijk} correlations to make up the full Ψ_V the energy by ~ 2.7 MeV, but requires ~ 2.7 times more computation than Ψ_P. However, about 60% of the energy gain can be obtained for only a 20% increase in computation by using the trial function Ψ_T defined by

TABLE III. Values of three-nucleon correlation parameters. Notation is same as Ref. [7].

ϵ_a	-0.00025
ϵ_c	-0.0004
ϵ_u	-0.0005
y	0.72
q_1^c (fm^{-6})	0.20
q_2^c (fm^{-1})	0.85
q_1^p	0.16
q_2^p (fm^{-1})	0.05
$q_1^{\ell s}$ (fm^{-2})	-0.12
$q_2^{\ell s}$ (fm^{-2})	0.12
$q_3^{\ell s}$ (fm^{-2})	0.85
q_1^τ (fm^{-1})	-0.012
q_2^τ (fm^{-2})	0.015
q_3^τ (fm)	1.2
q_4^τ	0.35

TABLE IV. Energy obtained with different trial functions for ^{6}Li in MeV, and relative cost to compute.

Wave function	E_V	δE	Cost
$|\Psi_P\rangle$	$-25.47(30)$		1.00
$|\Psi_T\rangle$	$-27.00(13)$	-1.53	1.19
$[1 + \Sigma_{i<j<k}U_{ijk}^{\text{TNI}}]|\Psi_P\rangle$	$-27.11(12)$	-1.64	1.59
$[1 + \Sigma_{i<j}U_{ij}^{LS} + \Sigma_{i<j<k}U_{ijk}^{\text{TNI}}]|\Psi_P\rangle$	$-27.89(12)$	-2.42	2.23
$|\Psi_V\rangle$	$-28.14(11)$	-2.67	2.66

$$|\Psi_T\rangle = \left[1 + \sum_{i<j<k} \widetilde{U}_{ijk}^{\text{TNI}}\right]|\Psi_P\rangle. \qquad (3.13)$$

Here $\widetilde{U}_{ijk}^{\text{TNI}}$ is a truncated TNI correlation from which the commutator term, $\epsilon_C V_{ijk}^C$, has been omitted:

$$\widetilde{U}_{ijk}^{\text{TNI}} = \widetilde{\epsilon}_A V_{ijk}^A + \epsilon_R V_{ijk}^R. \qquad (3.14)$$

The strength of the anticommutator term is increased to compensate, with $\widetilde{\epsilon}_A \sim 1.5\epsilon_A$. From Table IV we see that this simplification gets 90% of the gain of adding the full U_{ijk}^{TNI}, at $\frac{1}{3}$ the cost. The computer time is reduced so significantly because $\{X_{ij}^\pi, X_{jk}^\pi\}$ can be written as a generalized tensor operator involving the spins of only nucleons i and k; thus the time scales as the number of pairs rather than the number of triples. As discussed below, Ψ_T is in fact the most economical starting point for the GFMC calculations.

The Jastrow wave function for $A = 6$ nuclei is more complicated, as two nucleons must be placed in the p shell. We use LS coupling to obtain the desired JM value of a given state, as suggested in shell-model studies of p-shell nuclei [1]. Different possible LS combinations lead to multiple components in the Jastrow wave function. We also allow for the possibility that the central correlations $f_c(r_{ij})$ and f_{ijk}^c could depend upon the shells (s or p) occupied by the particles and on the LS coupling. The Jastrow wave function is taken as

$$|\Psi_J\rangle = \mathcal{A}\left\{ \left[\prod_{i<j<k\leqslant 4} f_{ijk}^{sss} \prod_{l<m\leqslant 4} f_{lm5}^{ssp} f_{lm6}^{ssp} \prod_{n\leqslant 4} f_{n56}^{spp}\right] \right.$$

$$\times \left[\prod_{i<j\leqslant 4} f_{ss}(r_{ij}) \prod_{k\leqslant 4} f_{sp}(r_{k5})f_{sp}(r_{k6})\right]$$

$$\left. \times \sum_{LS} (\beta_{LS} f_{pp}^{LS}(r_{56})|\Phi_6(LSJMTT_3)_{1234:56}\rangle)\right\}.$$

$$(3.15)$$

The operator $\mathcal{A}$ indicates an antisymmetric sum over all possible partitions of the six particles into four s-shell and two p-shell ones. For the two-body correlations we use $f_{ss}(r) = f_c(r)$ from the ^{4}He wave function, while

$$f_{sp}(r) = [a_{sp} + b_{sp}W(r)]f_c(r) + c_{sp}(1 - \exp[-(r/d_{sp})^2]), \qquad (3.16)$$

$$f_{pp}^{LS}(r) = [a_{pp} + b_{pp}W(r)]f_c(r) + c_{pp}^{LS}(1 - \exp[-(r/d_{pp})^2]). \qquad (3.17)$$

Here we have supplemented the $f_c(r)$ with a long-range tail and allowed for a short-range modification with a Woods-

TABLE V. Values of variational parameters in p-shell nuclei.

| | $A=6$ | | | $A=7$ | | |
	$^{1,3}S[2]$	$^{1,3}D[2]$	$^{1,3}P[11]$	$^2P[3]$	$^2F[3]$	$[21]$ & $[111]$
a_{sp}	0.0	0.0	0.0	1.0	1.0	1.0
b_{sp}	1.0	1.0	1.0	0.0	0.0	0.0
c_{sp}	0.9	0.9	0.9	0.85	0.85	0.85
d_{sp} (fm)	3.2	3.2	3.2	3.2	3.2	3.2
a_{pp}	1.0	1.0	1.0	1.0	1.0	1.0
b_{pp}	0.0	0.0	0.0	0.0	0.0	0.0
c_{pp}	0.1	0.1	0.4	0.1	0.1	0.4
d_{pp} (fm)	3.2	3.2	3.2	3.2	3.2	3.2
R_f (fm)	4.0	4.0	4.0	4.0	4.0	4.0
a_f (fm)	1.0	1.0	1.0	1.0	1.0	1.0
V_p (MeV)	-20.0	-18.0	-18.0	-20.0	-18.0	-18.0
R_p (fm)	4.0	4.0	4.0	4.0	4.0	4.0
a_p (fm)	1.5	1.5	1.5	1.5	1.5	1.5

Saxon factor, $W(r)=\{1+\exp[(r-R_f)/a_f]\}^{-1}$. The a_{sp}, b_{sp}, etc., are variational parameters, whose values are given in Table V. For the three-body correlations, our best present trial function has $f^{sss}_{ijk}=f^c_{ijk}$ as in Eq. (3.10), and $f^{ssp}_{ijk}=f^{spp}_{ijk}=1$.

The LS components of the single-particle wave function are given by

$$|\Phi_6(LSJMTT_3)_{1234:56}\rangle=|\Phi_4(0000)_{1234}\phi^{LS}_p(R_{\alpha5})\phi^{LS}_p(R_{\alpha6})$$

$$\times\{[Y_{1m_l}(\Omega_{\alpha5})Y_{1m_{l'}}(\Omega_{\alpha6})]_{LM_L}$$

$$\times[\chi_5(\tfrac{1}{2}m_s)\chi_6(\tfrac{1}{2}m'_s)]_{SM_S}\}_{JM}$$

$$\times[\nu_5(\tfrac{1}{2}t_3)\nu_6(\tfrac{1}{2}t'_3)]_{TT_3}\rangle. \quad (3.18)$$

The $\phi^{LS}_p(R_{\alpha k})$ are p-wave solutions of a particle of reduced mass $\frac{4}{5}m_N$ in an effective α-N potential. They are functions of the distance between the center of mass of the α core (which contains particles 1–4 in this partition) and nucleon k, and again may be different for different LS components. We use a Woods-Saxon potential well:

$$V_{\alpha N}(r)=V^{LS}_p\left[1+\exp\left(\frac{r-R_p}{a_p}\right)\right]^{-1}, \quad (3.19)$$

where V^{LS}_p, R_p, and a_p are variational parameters and we allow the depth of the well to vary with the LS composition. The values of these parameters are also given in Table V. The wave function is translationally invariant, hence there is no spurious center-of-mass motion.

The experimental spectra for $A=6$ nuclei [18] are shown in Fig. 1. The ground state of ^{6}He is strong stable, but decays by β^- emission with a mean life of 807 ms. The first

excited state is above the threshold for decay to $\alpha+n+n$ and has a width of ≈110 keV; we treat it here as a stable state with zero width. In the shell model, the $(J^\pi;T)=(0^+;1)$ ground state of ^{6}He is predominantly a $^{2S+1}L[n]=^1S[2]$ state, where we use spectroscopic notation to denote the total L and S of the state and the Young pattern $[n]$ to indicate the spatial symmetry. The $(2^+;1)$ first excited state is predominantly a $^1D[2]$ state. We allow for a possible $^3P[11]$ admixture in both states, using amplitudes β_{00} and β_{11} in the ground state, and β_{20} and β_{11} in the excited state. After other parameters in the trial function have been optimized, we make a series of calculations in which the β_{LS} may be different in the left- and right-hand-side wave functions to obtain the diagonal and off-diagonal matrix elements of the Hamiltonian and the corresponding normalizations and overlaps. We diagonalize the resulting 2×2 energy matrices to find the β_{LS} eigenvectors. The shell-model wave functions are orthonormal, but the correlated Ψ_V are not. Hence the diagonalizations use generalized eigenvalue routines including overlap matrices. We also calculate the position of the three complementary $^3P[11]$ states, with $(J^\pi;T)=(2^+;1)$, $(1^+;1)$, and $(0^+;1)$; only one of these has been tentatively identified experimentally [19]. The
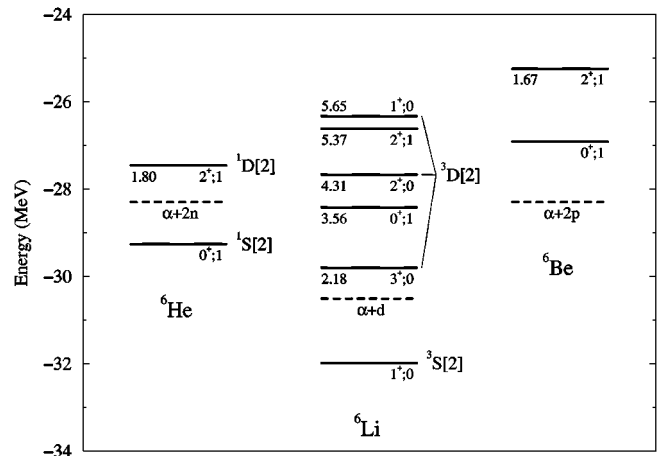

FIG. 1. The experimental spectrum for $A=6$ nuclei.

TABLE VI. β_{LSn} components in $A=6$ states, in order of increasing excitation for $T=0$ and $T=1$.

$(J^\pi;T)$	$^1S[2]$	$^3S[2]$	$^1D[2]$	$^3D[2]$	$^1P[11]$	$^3P[11]$
$(1^+,0)$		0.987		0.117	0.111	
$(3^+;0)$				1		
$(2^+;0)$				1		
$(1^+,0)$		-0.074		0.949	-0.306	
$(1^+,0)$		-0.153		0.300	0.942	
$(0^+;1)$	0.967					-0.253
$(2^+;1)$			0.880			0.476
$(2^+;1)$			-0.476			0.878
$(1^+;1)$						1
$(0^+;1)$	0.262					0.965

normalized β_{LS} for these different states are given in Table VI.

The spectrum for ^{6}Li contains a $(1^+;0)$ ground state that is predominantly $^3S[2]$ in character and a triplet of $^3D[2]$ excited states with $(3^+;0)$, $(2^+;0)$, and $(1^+;0)$ components. In addition, there are $(0^+;1)$ and $(2^+;1)$ excited states that are the isobaric analogs of the ^{6}He ground and excited states. The ^{6}Li ground state is stable, while the $(3^+;0)$ first excited state is above the threshold for breakup into $\alpha+d$, but is narrow with a width of 24 keV. The $(0^+;1)$ second excited state is even narrower, being unable to decay to $\alpha+d$ without isospin violation, and thus has a width of only 8 eV. The higher excitations have widths of 0.5 to 1.7 MeV, but we will treat them here as well-defined states. For the $(1^+;0)$ ground and excited states we mix β_{01}, β_{21}, and β_{10} amplitudes by diagonalizing a 3×3 energy matrix. The latter amplitude corresponds to an unobserved $^1P[11]$ state, which we also obtain in this diagonalization. However, only the β_{21} amplitude contributes to the $(3^+;0)$ and $(2^+;0)$ excited states. Again, Table VI gives a summary of the β_{LS} amplitudes.

The ground and first excited states in ^{6}Be have the same character as those in ^{6}He, except that the Coulomb interac-

tion makes the ground state a resonance, with a width of 92 keV. Again, we neglect the resonance character of these states in constructing the trial function. Most of the numerical results calculated here for the CIB terms of the Hamiltonian are obtained by interchanging neutrons and protons in the wave function. This does not allow for the changes expected in ^{6}Be compared to ^{6}He due to the Coulomb force, so we have also made some calculations adding a Coulomb term $V_{\alpha N}^C(r)$, folded over nuclear form factors, to the $V_{\alpha N}(r)$ used to generate the single-particle $\phi_p(R_{\alpha k})$ functions:

$$V_{\alpha N}^C(r) = Z\frac{e^2}{r}\left\{1-\frac{1}{2}\exp(-x_\alpha)\left[2+x_\alpha+\frac{4}{1-y^2}\right][1-y^{-2}]^{-2}\right.$$

$$\left.-\frac{1}{2}\exp(-x_p)\left[2+x_p+\frac{4}{1-y^{-2}}\right][1-y^2]^{-2}\right\}.$$

$$(3.20)$$

Here $x_\alpha=\sqrt{12}r/r_\alpha$, $x_p=\sqrt{12}r/r_p$, and $y=r_\alpha/r_p$, with the charge radii $r_\alpha=1.65$ fm and $r_p=0.81$ fm. This additional potential term can be used with strength $Z=0$, 1, or 2 for ^{6}He, ^{6}Li, or ^{6}Be, respectively, corresponding to the average Coulomb interaction between the α core and a p-shell nucleon.

The full $A=6$ wave function is constructed by acting on the $|\Psi_J\rangle$, Eq. (3.15), with the same U_{ij}, U_{ij}^{LS}, U_{ijk}, and U_{ijk}^{TNI} correlations used in ^{4}He. The one exception is that the optimal strength of the U_{ijk} correlations is reduced slightly as A increases. In principle, the U_{ij} could be generalized to be different according to whether particles i and j are in the s or p shell, but this would require a larger sum over the different partitions and would increase the computational cost by an order of magnitude.

The Jastrow wave function for $A=7$ nuclei is a straightforward extension of Eq. (3.15), with the added specification of the spatial symmetry $[n]$ of the angular momentum coupling of three p-shell nucleons:

$$|\Psi_J\rangle = \mathcal{A}\left\{\left[\prod_{i<j<k\leq 4} f_{ijk}^{sss}\prod_{l<m\leq 4} f_{lm5}^{ssp}f_{lm6}^{ssp}f_{lm7}^{ssp}\prod_{n\leq 4} f_{n56}^{spp}f_{n57}^{spp}f_{n67}^{spp}f_{567}^{ppp}\right]\right.$$

$$\left.\times\left[\prod_{i<j\leq 4} f_{ss}(r_{ij})\prod_{k\leq 4} f_{sp}(r_{k5})f_{sp}(r_{k6})f_{sp}(r_{k7})\sum_{LS[n]}\left(\beta_{LS[n]}\prod_{5\leq l<m} f_{pp}^{LS}(r_{lm})|\Phi_7(LS[n]JMTT_3)_{1234:567}\rangle\right)\right]\right\}.$$

$$(3.21)$$

The single-particle wave function is then

$$|\Phi_7(LS[n]JMTT_3)_{1234:567}\rangle = |\Phi_4(0000)_{1234}\phi_p^{LS}(R_{\alpha 5})\phi_p^{LS}(R_{\alpha 6})\phi_p^{LS}(R_{\alpha 7})$$

$$\times\{[Y_{1m_l}(\Omega_{\alpha 5})Y_{1m_{l'}}(\Omega_{\alpha 6})Y_{1m_l''}(\Omega_{\alpha 7})]_{LM_L[n]}[\chi_5(\tfrac{1}{2}m_s)\chi_6(\tfrac{1}{2}m_s')\chi_7(\tfrac{1}{2}m_s'')]_{SM_S}\}_{JM}$$

$$\times[\nu_5(\tfrac{1}{2}t_3)\nu_6(\tfrac{1}{2}t_3')\nu_7(\tfrac{1}{2}t_3'')]_{TT_3}\rangle.$$
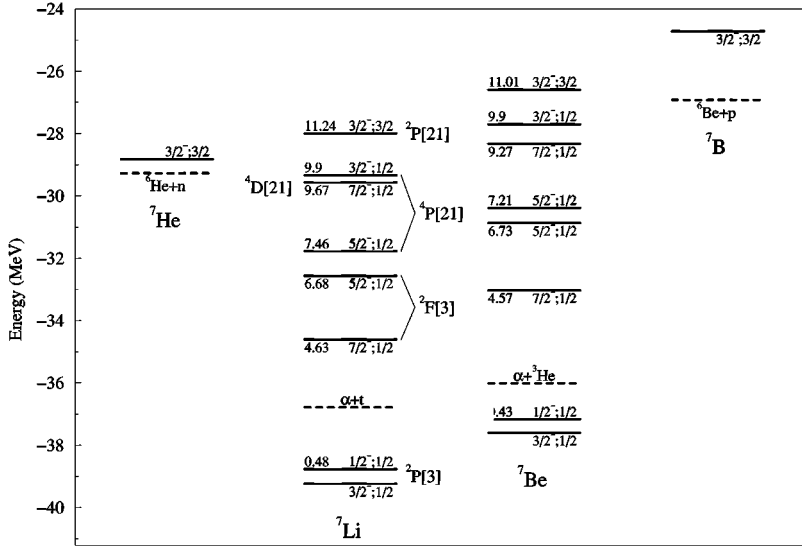
$$(3.22)$$

FIG. 2. The experimental spectrum for $A=7$ nuclei.

There is an implicit complementary symmetry $[n']$ for the spin-isospin part of the wave function, to preserve the overall antisymmetry, which we do not show here explicitly; for a detailed discussion of the symmetry considerations see Appendix 1C of Ref. [20]. The full wave function is again built up using Eq. (3.2) with the added definition of the central p-shell three-body correlation $f_{ijk}^{ppp}=f_{ijk}^{sss}$.

The experimental spectra for $A=7$ nuclei [18] are shown in Fig. 2. In the shell model, the lowest states for the $T=\frac{1}{2}$ nuclei ^{7}Li and ^{7}Be have a predominantly $^2P[3]$ character, split into $(J^\pi;T)=(\frac{3}{2}^-,\frac{1}{2})$ ground and $(\frac{1}{2}^-,\frac{1}{2})$ first excited states. These states are all strong stable, the first excited states having mean lives $\approx 100-200$ fs, while the ground state of ^{7}Be decays weakly with a mean life of 53 days. Each ground state can also have contributions with a mixed spatial symmetry, including $^2P[21]$, $^4P[21]$, $^4D[21]$, and $^2D[21]$ components, while the first excited state has admixtures of $^2P[21]$, $^4P[21]$, $^4D[21]$, and $^2S[111]$ amplitudes. We have diagonalized 5×5 matrices for these states. Higher in the spectrum is a predominantly $^2F[3]$ state that splits into

$(\frac{7}{2}^-,\frac{1}{2})$ and $(\frac{5}{2}^-,\frac{1}{2})$ pieces. The lower state is mixed with a $^4D[21]$ component, while the upper state has $^4P[21]$, $^4D[21]$, and $^2D[21]$ contributions. Again we have performed diagonalizations in the $\beta_{LS[n]}$ amplitudes to project out the lowest $(\frac{7}{2}^-,\frac{1}{2})$ and $(\frac{5}{2}^-,\frac{1}{2})$ states.

The diagonalizations confirm that the ground and first excited states are almost pure $^2P[3]$ and the second and third excited states are almost pure $^2F[3]$. We have also calculated the next excited state of each J as given by our projections to confirm that they lie above these first four states. The normalized amplitudes of the lowest two states of each J are given in Table VII. These higher excitations include a triplet of predominantly $^4P[21]$ states: $(\frac{5}{2}^-,\frac{1}{2})$, $(\frac{3}{2}^-,\frac{1}{2})$, and $(\frac{1}{2}^-,\frac{1}{2})$, and a $(\frac{7}{2}^-,\frac{1}{2})$ state that is predominantly $^4D[21]$. The experimental spectrum shows a similar ordering of states, except that the $(\frac{7}{2}^-,\frac{1}{2})$ comes in the midst of the $^4P[21]$ states, and no second $(\frac{1}{2}^-,\frac{1}{2})$ state has been identified in this range of energy excitation.

The spectrum for $T=\frac{3}{2}$ states in $A=7$ nuclei is also shown

TABLE VII. β_{LSn} components in $A=7$ states, in order of increasing excitation for $T=\frac{1}{2}$ and $T=\frac{3}{2}$.

$(J^\pi;T)$	$^2P[3]$	$^2F[3]$	$^2P[21]$	$^4P[21]$	$^2D[21]$	$^4D[21]$	$^2S[111]$	$^4S[111]$
$(\frac{3}{2}^-,\frac{1}{2})$	0.998		0.001	0.050	-0.041	0.012		
$(\frac{1}{2}^-,\frac{1}{2})$	0.994		-0.087	0.001		-0.068	-0.010	
$(\frac{7}{2}^-,\frac{1}{2})$		0.998				0.059		
$(\frac{5}{2}^-,\frac{1}{2})$		0.995		0.073	-0.060	0.036		
$(\frac{5}{2}^-,\frac{1}{2})$		-0.059		0.969	0.168	-0.171		
$(\frac{7}{2}^-,\frac{1}{2})$		-0.052				0.999		
$(\frac{3}{2}^-,\frac{1}{2})$	-0.041		-0.022	0.998	0.039	-0.015		
$(\frac{1}{2}^-,\frac{1}{2})$	0.035		0.412	0.909		-0.014	-0.057	
$(\frac{3}{2}^-,\frac{3}{2})$			0.864		0.480			-0.153
$(\frac{1}{2}^-,\frac{3}{2})$			1					
$(\frac{5}{2}^-,\frac{3}{2})$					1			
$(\frac{3}{2}^-,\frac{3}{2})$			-0.448		0.841			0.303

in Fig. 2. The $(\frac{3}{2}^-;\frac{3}{2})$ ground state for ^{7}He is 0.44 MeV above the threshold for breakup into ^{6}He$+n$ with a width of 160 keV. The isobaric analogs have widths of 260, 320, and 1200 keV for ^{7}Li, ^{7}Be, and ^{7}B, respectively. This state can have contributions from $^2P[21]$, $^2D[21]$, and $^4S[111]$ amplitudes, and we again diagonalize a 3×3 matrix to evaluate the $\beta_{LS[n]}$ components, as shown in Table VII. We also calculate the first three excited states: a $(\frac{1}{2}^-;\frac{3}{2})$ $^2P[21]$ state, a $(\frac{5}{2}^-;\frac{3}{2})$ $^2D[21]$ state, and the second mixed $(\frac{3}{2}^-;\frac{3}{2})$ state. None of these excited states have been experimentally identified.

B. Energy evaluation

The energy expectation value of Eq. (3.1) is evaluated using Monte Carlo integration. A detailed technical description of the methods used here can be found in Refs. [17,21,22]. Monte Carlo sampling is done both in configuration space and in the order of operators in the symmetrized product of Eq. (3.3) by following a Metropolis random walk. The expectation value for an operator O is given by

$$\langle O\rangle = \frac{\sum_{p,q}\int d\mathbf{R}\,\Psi_p^\dagger(\mathbf{R})O\Psi_q(\mathbf{R})}{\sum_{p,q}\int d\mathbf{R}\,\Psi_p^\dagger(\mathbf{R})\Psi_q(\mathbf{R})}. \qquad (3.23)$$

The subscripts p and q specify the order of operators in the left- and right-hand side wave functions, while the integration runs over the particle coordinates $\mathbf{R}=(\mathbf{r}_1,\mathbf{r}_2,\ldots,\mathbf{r}_A)$. This multidimensional integration is facilitated by introducing a probability distribution, $W_{pq}(\mathbf{R})$, such that

$$\langle O\rangle = \frac{\sum_{p,q}\int d\mathbf{R}[\Psi_p^\dagger(\mathbf{R})O\Psi_q(\mathbf{R})/W_{pq}(\mathbf{R})]W_{pq}(\mathbf{R})}{\sum_{p,q}\int d\mathbf{R}[\Psi_p^\dagger(\mathbf{R})\Psi_q(\mathbf{R})/W_{pq}(\mathbf{R})]W_{pq}(\mathbf{R})}. $$
$$(3.24)$$

This probability distribution is taken to be

$$W_{pq}(\mathbf{R}) = |\text{Re}(\langle\Psi_{P,p}^\dagger(\mathbf{R})\Psi_{P,q}(\mathbf{R})\rangle)|, \qquad (3.25)$$

which is constructed from the pair wave function, Ψ_P, but with only one operator order of the symmetrized product. This probability distribution is much less expensive to compute than the full wave function of Eq. (3.2) with its spin-orbit and operator-dependent three-body correlations, but it typically has a norm within 1–2 % of the full wave function.

Expectation values have a statistical error which can be estimated by the standard deviation σ:

$$\sigma = \left[\frac{\langle O^2\rangle - \langle O\rangle^2}{N-1}\right]^{1/2}, \qquad (3.26)$$

where N is the number of statistically independent samples. Block averaging schemes can be used to estimate the autocorrelation times and determine the statistical error.

The wave function Ψ can be represented by an array of $2^A\times\binom{A}{Z}$ complex numbers,

$$\Psi(\mathbf{R}) = \sum_\alpha \psi_\alpha(\mathbf{R})|\alpha\rangle, \qquad (3.27)$$

where the $\psi_\alpha(\mathbf{R})$ are the coefficients of each state $|\alpha\rangle$ with specific third components of spin and isospin. This gives arrays with 96, 960, 1280, 2688, and 4480 elements for ^{4}He, ^{6}He, ^{6}Li, ^{7}He, and ^{7}Li, respectively. The spin, isospin, and tensor operators $O_{ij}^{p=2,6}$ contained in the two-body correlation operator U_{ij}, and in the Hamiltonian are sparse matrices in this basis. For forces that are largely charge independent, as is the case here, we can replace this charge-conserving basis with an isospin-conserving basis that has $N(A,T) = 2^A\times I(A,T)$ components, where

$$I(A,T) = \frac{2T+1}{\frac{1}{2}A+T+1}\begin{pmatrix} A \\ \frac{1}{2}A+T \end{pmatrix}. \qquad (3.28)$$

This reduces the number of array elements to 32, 576, 320, 1792, and 1792 for the cases given above—a significant savings. In practice, the $\tau_i\cdot\tau_j$ operator is more expensive to evaluate in this basis, but the overall savings in computation are still large.

Expectation values of the kinetic energy and spin-orbit potential require the computation of first derivatives and diagonal second derivatives of the wave function. These are obtained by evaluating the wave function at $6A$ slightly shifted positions of the coordinates $\mathbf{R}$ and taking finite differences, as discussed in Ref. [17]. Potential terms quadratic in $\mathbf{L}$ require mixed second derivatives, which can be obtained by additional wave function evaluations and finite differences. A rotation trick can be used to reduce the number of additional locations at which the wave function must be evaluated [23].

As a check on the correctness of our Monte Carlo integration, we have evaluated the energy expectation value $\langle H\rangle$ for the deuteron using the exact wave function as input, and match the energy to better than 1 keV. We have made similar calculations for the triton using a Faddeev wave function, as discussed in Ref. [17], and obtained agreement with independent Faddeev calculations at the 10–20 keV level. For the much more complicated $A=6,7$ wave functions, we also evaluate the expectation values $\langle J^2\rangle$ and $\langle J_z\rangle$ to verify that they truly have the specified quantum numbers. A third check is made on the antisymmetry of the Jastrow wave function by evaluating, at an initial randomized position,

$$\frac{\Psi_J^\dagger[1+P_{ij}^x P_{ij}^\sigma P_{ij}^\tau]\Psi_J}{\Psi_J^\dagger\Psi_J}, \qquad (3.29)$$

where $P_{ij}^{x,\sigma,\tau}$ are the space, spin, and isospin exchange operators. This value should be exactly zero for an antisymmetric wave function, and it is in fact less than 10^{-9} for each pair of particles in each nuclear state that we study.

A major problem arises in minimizing the variational energy for p-shell nuclei using the above wave functions: there is no variational minimum that gives reasonable rms radii. For example, the variational energy for ^{6}Li is slightly more

bound than for ^{4}He, but is not more bound than for separated ^{4}He and ^{2}H nuclei, so the wave function is not stable against breakup into $\alpha + d$ subclusters. Consequently, the energy can be lowered toward the sum of ^{4}He and ^{2}H energies by making the wave function more and more diffuse. Such a diffuse wave function would not be useful for computing other nuclear properties, or as a starting point for the GFMC calculation (see Sec. VI below), so we constrain our search for optimal variational parameters by requiring the resulting point proton rms radius, r_p, to be close to the experimental values for ^{6}Li and ^{7}Li ground states. For ^{6}He and ^{7}Be ground states, and all the excited or resonant states, there are no experimental measurements of the charge radii. To avoid introducing too many additional parameter values, we construct these wave functions by making minimal changes to the ^{6}Li and ^{7}Li wave functions, with the added requirement that the excited states should not have smaller radii than the ground states.

For $A = 6$ nuclei, we begin by selecting parameters to minimize the energy of the ^{6}Li $^3S[2]$ component (the dominant part of the ground state) subject to the constraint that $r_p \sim 2.4 - 2.5$ fm. For the other components, only the depth of the single-particle well, V_p^{LS}, of Eq. (3.19), and the tail, c_{pp}^{LS}, of the p-shell pair-correlation function of Eq. (3.17) are varied, as shown in Table V. The well depth for the $^3D[2]$ states is decreased to get the rms radius of the $(3^+; 0)$ excited state larger than the ground state. The tail is increased for the mixed-symmetry $^1P[11]$ state for the same reason. For ^{6}He we use the same parameters as in ^{6}Li for the corresponding $^1S[2]$, $^1D[2]$, and $^3P[11]$ states. The only other difference between ^{6}Li and ^{6}He wave functions is that we may turn on the α-N Coulomb potential of Eq. (3.20) when generating the single-particle radial functions ϕ_p. Finally, the diagonalizations are made to determine the β_{LS} mixing coefficients of Table VI.

A similar procedure is followed for the $A = 7$ nuclei. Parameters are selected for the dominant $^2P[3]$ state in ^{7}Li subject to the constraint that $r_p \sim 2.2 - 2.3$ fm. The well depth is reduced for the $^2F[3]$ states, and the tail is increased for all the mixed-symmetry states. Afterwards the β_{LS} diagonalization is carried out. Since ^{7}Be is a mirror nucleus, it has the same wave function as ^{7}Li, aside from changing the α-N Coulomb potential. The ^{7}He and ^{7}B ground states are isobaric analogs to mixed symmetry states in ^{7}Li, so they use corresponding parameters.

Shell-model lore tells us that the lowest state of any given $(J^\pi; T)$ will be the state with maximal spatial symmetry and smallest L that can be formed from the allowed couplings, e.g., the $^3S[2]$ ground state in ^{6}Li or the $^2P[3]$ ground state in ^{7}Li. For the purposes of obtaining a variational upper bound and a GFMC starting point, we could settle for a Ψ_V constructed using only that $LS[n]$ component. However, by using all the allowed components, we can gain a significant amount of energy in some cases and, as is discussed below, this gain persists in our GFMC propagations. For the $A = 6$ nuclei, the diagonalizations for the $(0^+; 1)$, $(1^+; 0)$, and $(2^+; 1)$ states improve the lower state by 0.25 to 0.5 MeV. In the first four ^{7}Li $T = \frac{1}{2}$ states, the mixing is much less, and improvements are at most 0.15 MeV. However, for ^{7}He,

there is a gain of 0.75 MeV, probably because there are two states of identical symmetry that only differ by 1 in L.

The diagonalizations have the additional benefit that we can predict where the next higher excited state of each $(J^\pi; T)$ lies. This allows us to confirm that the Hamiltonian is not predicting any unusually low excitations that are not observed experimentally; e.g., the second $(\frac{3}{2}^-; \frac{1}{2})$ and $(\frac{1}{2}^-; \frac{1}{2})$ states in ^{7}Li do not appear below the first $(\frac{7}{2}^-; \frac{1}{2})$ and $(\frac{5}{2}^-; \frac{1}{2})$ states.

IV. GREEN'S FUNCTION MONTE CARLO

The aim of the GFMC method is to project out the exact lowest energy state, Ψ_0, associated with a chosen set of quantum numbers, from an approximation Ψ_T to that state. The method used here is essentially identical to that used previously to calculate nuclei with $A \leq 6$ [4], with the exception that we have now incorporated the exact two-body propagator in the imaginary-time propagation. In this section we describe the algorithm in some detail, in particular relating it to algorithms commonly used for scalar interactions. For simplicity of notation we will not make the distinction between H' and H (and their respective components) that was introduced with Eq. (2.17); the reader will want to remember that we in fact use the simpler H' in our GFMC propagator.

GFMC projects out the lowest energy ground state using $\Psi_0 = \lim_{\tau \to \infty} \exp[-(H - E_0)\tau]\Psi_T$. The eigenvalue E_0 is calculated exactly while other expectation values are generally calculated neglecting terms of order $|\Psi_0 - \Psi_T|^2$ and higher. In contrast, the error in the variational energy, E_V, is of order $|\Psi_0 - \Psi_T|^2$, and other expectation values calculated with Ψ_T have errors of order $|\Psi_0 - \Psi_T|$.

We use the Ψ_T of Eq. (3.13) as our initial trial function and define the propagated wave function $\Psi(\tau)$ as

$$\Psi(\tau) = e^{-(H - E_0)\tau}\Psi_T; \tag{4.1}$$

obviously $\Psi(\tau = 0) = \Psi_T$ and $\Psi(\tau \to \infty) = \Psi_0$. Introducing a small time step, $\Delta\tau$, $\tau = n\Delta\tau$, gives

$$\Psi(\tau) = [e^{-(H - E_0)\Delta\tau}]^n\Psi_T. \tag{4.2}$$

The $\Psi(\tau)$ is represented by a vector function of $\mathbf{R}$ using Eq. (3.27), and the Green's function, $G_{\alpha\beta}(\mathbf{R}, \mathbf{R}')$ is a matrix function of $\mathbf{R}$ and $\mathbf{R}'$ in spin-isospin space, defined as

$$G_{\alpha\beta}(\mathbf{R}, \mathbf{R}') = \langle \mathbf{R}, \alpha | e^{-(H - E_0)\Delta\tau} | \mathbf{R}', \beta \rangle. \tag{4.3}$$

It is calculated with leading errors of order $(\Delta\tau)^3$ as discussed in Sec. IV B. The errors in the full calculation are determined by the difference between the (artificial) Hamiltonian for which the propagator is exact and H. This difference is of order $(\Delta\tau)^2$, and $\Delta\tau$ is chosen to be small enough that this total error is negligible. Omitting spin-isospin indices for brevity, $\Psi(\mathbf{R}_n, \tau)$ is given by

$$\Psi(\mathbf{R}_n, \tau) = \int G(\mathbf{R}_n, \mathbf{R}_{n-1}) \cdots G(\mathbf{R}_1, \mathbf{R}_0)\Psi_T(\mathbf{R}_0)$$
$$\times d\mathbf{R}_{n-1} \cdots \mathbf{R}_1 d\mathbf{R}_0. \tag{4.4}$$

The mixed expectation value of an operator O is defined as

$$\langle O \rangle_{\text{Mixed}} = \frac{\langle \Psi_T | O | \Psi(\tau) \rangle}{\langle \Psi_T | \Psi(\tau) \rangle} = \frac{\int d\mathbf{P}_n \Psi_T^\dagger(\mathbf{R}_n) O G(\mathbf{R}_n, \mathbf{R}_{n-1}) \cdots G(\mathbf{R}_1, \mathbf{R}_0) \Psi_T(\mathbf{R}_0)}{\int d\mathbf{P}_n \Psi_T^\dagger(\mathbf{R}_n) G(\mathbf{R}_n, \mathbf{R}_{n-1}) \cdots G(\mathbf{R}_1, \mathbf{R}_0) \Psi_T(\mathbf{R}_0)}, \tag{4.5}$$

where $\mathbf{P}_n = \mathbf{R}_0, \mathbf{R}_1, \cdots, \mathbf{R}_n$ denotes the "path," and

$$d\mathbf{P}_n = d\mathbf{R}_0 d\mathbf{R}_1 \cdots d\mathbf{R}_n. \tag{4.6}$$

In GFMC, the integral over the paths is carried out stochastically. Generally, the required expectation values are calculated approximately from the variational Ψ_T and mixed expectation values. Let

$$\Psi(\tau) = \Psi_T + \delta\Psi(\tau). \tag{4.7}$$

Retaining only the terms of order $\delta\Psi(\tau)$, we obtain

$$\langle O(\tau) \rangle = \frac{\langle \Psi(\tau) | O | \Psi(\tau) \rangle}{\langle \Psi(\tau) | \Psi(\tau) \rangle}$$
$$\approx \langle O(\tau) \rangle_{\text{Mixed}} + [\langle O(\tau) \rangle_{\text{Mixed}} - \langle O \rangle_T], \tag{4.8}$$

where

$$\langle O \rangle_T = \frac{\langle \Psi_T | O | \Psi_T \rangle}{\langle \Psi_T | \Psi_T \rangle}. \tag{4.9}$$

More accurate evaluations of $\langle O(\tau) \rangle$ are possible, [24] essentially by measuring the observable at the midpoint of the path. However, such estimates require a propagation twice as long as the mixed estimate. Since we are limited in the present calculations to a total propagation time of 0.06 MeV^{-1}, we use the approximation (4.8).

An important exception to the above is the energy, E_0 given by $\langle H(\tau \to \infty) \rangle$. The $\langle H(\tau) \rangle_{\text{Mixed}}$ can be reexpressed as (Ref. [25])

$$\langle H(\tau) \rangle_{\text{Mixed}} = \frac{\langle \Psi_T | e^{-(H-E_0)\tau/2} H e^{-(H-E_0)\tau/2} | \Psi_T \rangle}{\langle \Psi_T | e^{-(H-E_0)\tau/2} e^{-(H-E_0)\tau/2} | \Psi_T \rangle}, \tag{4.10}$$

since the propagator $\exp[-(H-E_0)\tau]$ commutes with the Hamiltonian. Thus $\langle H(\tau) \rangle_{\text{Mixed}}$ approaches E_0 in the limit $\tau \to \infty$, and furthermore, being an expectation value of H, it obeys the variational principle

$$\langle H(\tau) \rangle_{\text{Mixed}} \geq E_0. \tag{4.11}$$

If a simpler H' is being used to construct the GFMC propagator, then these equations apply to $\langle H'(\tau) \rangle$, and $\langle (H-H') \rangle$ must be evaluated using Eq. (4.8).

Given these expressions, two basic elements are required for any GFMC calculation. The first element is the choice of short-time propagator $\exp[-(H-E_0)\Delta\tau]$ and the second is a method for sampling the paths. We discuss each of these elements in turn.

A. The short-time propagator

The short-time propagator should allow as large a time step $\Delta\tau$ as possible, since the total computational time for propagation is proportional to $1/\Delta\tau$. Earlier calculations [4,26,8] used the propagator obtained from the Feynman formulas. Ignoring three-nucleon interaction terms in H, it is given by

$$e^{-H\Delta\tau} = \left[\mathcal{S} \prod_{i<j} e^{-v_{ij}\Delta\tau/2} \right] e^{-K\Delta\tau} \left[\mathcal{S} \prod_{i<j} e^{-v_{ij}\Delta\tau/2} \right] + \mathcal{O}(\Delta\tau^3). \tag{4.12}$$

Note that it is useful to symmetrize the product of $e^{-v_{ij}\Delta\tau/2}$ when $[v_{ij}, v_{jk}] \neq 0$, in order to reduce the error per iteration. The nuclear v_{ij} has a repulsive core of order GeV. The main error in the above propagator comes from terms in $e^{-H\Delta\tau}$ having multiple v_{ij}, like $v_{ij} K v_{ij} (\Delta\tau)^3$ for example, which can become large when particles i and j are very close. In order to make them negligible a rather small $\Delta\tau \sim 0.1$ GeV^{-1} is used with the above propagator. The matrix elements of the propagator are given by

$$G_{\alpha\beta}(\mathbf{R}, \mathbf{R}') = G_0(\mathbf{R}, \mathbf{R}') \langle \alpha | \left[\mathcal{S} \prod_{i<j} e^{-v_{ij}(\mathbf{r}_{ij})\Delta\tau/2} \right]$$
$$\times \left[\mathcal{S} \prod_{i<j} e^{-v_{ij}(\mathbf{r}'_{ij})\Delta\tau/2} \right] | \beta \rangle, \tag{4.13}$$

$$G_0(\mathbf{R}, \mathbf{R}') = \langle \mathbf{R} | e^{-K\Delta\tau} | \mathbf{R}' \rangle$$
$$= \left[\sqrt{\frac{m}{2\pi\hbar^2\Delta\tau}} \right]^{3A} \exp\left[\frac{-(\mathbf{R}-\mathbf{R}')^2}{2\hbar^2\Delta\tau/m} \right]. \tag{4.14}$$

However, it is well known from the studies of bulk helium atoms [27] that including the exact two-body propagator allows much larger time steps. This short-time propagator is

$$G_{\alpha\beta}(\mathbf{R}, \mathbf{R}') = G_0(\mathbf{R}, \mathbf{R}') \langle \alpha | \left[\mathcal{S} \prod_{i<j} \frac{g_{ij}(\mathbf{r}_{ij}, \mathbf{r}'_{ij})}{g_{0,ij}(\mathbf{r}_{ij}, \mathbf{r}'_{ij})} \right] | \beta \rangle, \tag{4.15}$$

where g_{ij} is the exact two-body propagator,

$$g_{ij}(\mathbf{r}_{ij}, \mathbf{r}'_{ij}) = \langle \mathbf{r}_{ij} | e^{-H_{ij}\Delta\tau} | \mathbf{r}'_{ij} \rangle, \tag{4.16}$$

$$H_{ij} = -\frac{\hbar^2}{m} \nabla_{ij}^2 + v_{ij}, \tag{4.17}$$

and $g_{0,ij}$ is the free two-body propagator,

$$g_{0,ij}(\mathbf{r}_{ij},\mathbf{r}'_{ij}) = \left[\sqrt{\frac{\mu}{2\pi\hbar^2\Delta\tau}}\right]^3 \exp\left[-\frac{(\mathbf{r}_{ij}-\mathbf{r}'_{ij})^2}{2\hbar^2\Delta\tau/\mu}\right],$$

(4.18)

where $\mu = m/2$ is the reduced mass. All terms containing any number of the same v_{ij} and K are treated exactly in this propagator, as we have included the imaginary-time equivalent of the full two-body scattering amplitude. It still has errors of order $(\Delta\tau)^3$, however they are from commutators of terms like $v_{ij}Tv_{ik}(\Delta\tau)^3$ which become large only when both pairs ij and ik are close. Since this is a rare occurrence, a five times larger time step $\Delta\tau \sim 0.5$ GeV^{-1} can be used for the present studies of light nuclei. In the case of bound states of helium atoms a ~ 30 times larger time step can be used with the propagator (4.15) than with Eq. (4.12) presumably because the interatomic potentials have a relatively harder core, and they commute with each other.

Finally, including the three-body forces and the E_0 in Eq. (4.3), the complete propagator is given by

$$G_{\alpha\beta}(\mathbf{R},\mathbf{R}') = e^{E_0\Delta\tau}G_0(\mathbf{R},\mathbf{R}')\exp\left[-\sum\ [V^R_{ijk}(\mathbf{R})\right.$$

$$\left. + V^R_{ijk}(\mathbf{R}')]\frac{\Delta\tau}{2}\right]\langle\alpha|I_3(\mathbf{R})|\gamma\rangle$$

$$\times\left\langle\gamma\left|\left[\mathcal{S}\prod_{i<j}\frac{g_{ij}(\mathbf{r}_{ij},\mathbf{r}'_{ij})}{g_{0,ij}(\mathbf{r}_{ij},\mathbf{r}'_{ij})}\right]\right|\delta\right\rangle\langle\delta|I_3(\mathbf{R}')|\beta\rangle,$$

(4.19)

$$I_3(\mathbf{R}) = \left[1 - \frac{\Delta\tau}{2}\sum\ V^{2\pi}_{ijk}(\mathbf{R})\right].$$

(4.20)

The exponential of $V^{2\pi}_{ijk}$ is expanded to first order in $\Delta\tau$ thus, there are additional error terms of the form $V^{2\pi}_{ijk}V^{2\pi}_{i'j'k'}(\Delta\tau)^2$. However, they have negligible effect since $V^{2\pi}_{ijk}$ has a magnitude of only a few MeV. It was verified that the results for ^{4}He do not show any change, outside of statistical errors, when $\Delta\tau$ is decreased from 0.5 GeV^{-1}.

B. Calculation of g_{ij}

The pair propagator g_{ij} is a matrix in the two-body spin-isospin space, and obeys the equation

$$\left[\frac{\partial}{\partial\tau}+H_{ij}\right]g_{ij}(\mathbf{r},\mathbf{r}';\tau) = 0.$$

(4.21)

As the Hamiltonian naturally decomposes into eigenstates of the two-body spin and isospin, so does the propagator g_{ij}. In addition, it obeys the convolution equation

$$g_{ij}(\mathbf{r},\mathbf{r}';\tau+\tau') = \int d^3\mathbf{r}'\ g_{ij}(\mathbf{r},\mathbf{r}'';\tau)g_{ij}(\mathbf{r}'',\mathbf{r}';\tau'),$$

(4.22)

with the initial condition

$$g_{ij}(\mathbf{r},\mathbf{r}';\tau=0) = \delta(\mathbf{r},\mathbf{r}').$$

(4.23)

To calculate g_{ij}, we use the techniques developed by Schmidt and Lee [28] for scalar interactions. The basic idea is to use the convolution equation, Eq. (4.22), to write g_{ij} as a product over N steps:

$$g_{ij}(\mathbf{r}_N,\mathbf{r}_0;\Delta\tau) = \prod_{i=1}^{N}\ g_{ij}(\mathbf{r}_i,\mathbf{r}_{i-1};\epsilon),$$

(4.24)

with $\epsilon = \Delta\tau/N$ and an implied integration over intermediate points. If we use a symmetric expression for the short-time propagator $g_{ij}(\epsilon)$ such as

$$g_{ij}(\mathbf{r},\mathbf{r}';\epsilon) = e^{-v_{ij}(\mathbf{r})\epsilon/2}g_{0,ij}(\mathbf{r},\mathbf{r}';\epsilon)e^{-v_{ij}(\mathbf{r}')\epsilon/2},\ (4.25)$$

the errors for $g_{ij}(\Delta\tau)$ contain only even powers of $1/N$, starting with $1/N^2$ [28]. By evaluating $g_{ij}(\mathbf{r},\mathbf{r}';\Delta\tau)$ for several values of N (and consequently ϵ) and extrapolating to $\epsilon\to 0$ the g_{ij} can be calculated with high ($\sim$ 10 digit) accuracy.

Evaluation of g_{ij} can be carried out in various ways. We have chosen to expand the propagator in partial waves denoted by JM, TT_z, S, and L, thus replacing the three-dimensional integral in Eq. (4.22) with many one-dimensional integrals. The two-nucleon interaction v_{ij} has a simple form, $v^{LL'}_{JTS}(r)$, in these partial waves. The interaction is diagonal ($L=L'$) in $S=0$ and 1 waves with $L=J$, and it couples the $S=1$, L, $L'=J\pm 1$ waves.

The $g_{ij}(\mathbf{r},\mathbf{r}';\Delta\tau)$ is written as a sum over partial waves,

$$g_{ij}(\mathbf{r},\mathbf{r}';\Delta\tau) = \sum_{JM}\ \sum_{TT_z}\ \sum_{SLL'}\ \chi_{T,T_z}\mathcal{Y}^M_{JLS}(\hat{\mathbf{r}})$$

$$\times\frac{g^{LL'}_{JTS}(r,r';\Delta\tau)}{rr'}\mathcal{Y}^{\dagger M}_{JL'S}(\hat{\mathbf{r}}')\chi^{\dagger}_{T,T_z},$$

(4.26)

where χ_{T,T_z} denote isospin states, and $\mathcal{Y}^M_{JLS}(\hat{\mathbf{r}})$ are standard spin-angle functions that depend upon spins and the directions $\hat{\mathbf{r}}$ and $\hat{\mathbf{r}}'$. In uncoupled channels the partial wave propagators $g^{LL'}_{JTS}(r,r';\Delta\tau)$ are scalar functions of the magnitudes r and r', while for coupled channels they are 2×2 matrix functions with $L,L'=J\pm 1$. The partial wave propagators obey the one-dimensional convolution equation

$$g^{LL'}_{JTS}(r,r';\tau+\epsilon) = \int dr''\exp\left[-v^{LL''}_{JTS}(r)\frac{\epsilon}{2}\right]g^{L''}_{0,ij}(r,r'';\epsilon)$$

$$\times\exp\left[-v^{L''L'''}_{JTS}(r'')\frac{\epsilon}{2}\right]g^{L'''L'}_{JTS}(r'',r';\tau),$$

(4.27)

where $g^L_{0,ij}$ is the free propagator in partial waves with angular momentum L,

$$g^L_{0,ij} = \frac{x}{\sqrt{rr'}}I_L(x),$$

(4.28)

with

$$x \equiv \frac{rr'\mu}{2\hbar^2\tau}.$$

(4.29)

These expressions are used to obtain $g_{JTS}^{LL'}(r,r';\tau)$ for several values of ϵ, extrapolating to $\epsilon \to 0$ until a specific error tolerance has been reached. It is important to obtain these ''channel'' propagators very accurately, because they must be summed to reproduce a Gaussian falloff in the angular variables that is present in the full propagator. Fast-Fourier transforms are used to switch between momentum and coordinate space, where the kinetic and potential terms, respectively, are diagonal and can be trivially exponentiated.

We then sum over partial waves to obtain the full two-body propagator. If we were to include only the (physical) antisymmetric two-body channels, the complete two-body propagator would also be antisymmetric, and hence for small τ the propagator would have two peaks, one near the original point and another (with a minus sign in symmetric spin-isospin states), near the point corresponding to the interchange of the particles. In principle we could use this propagator by sampling paths with an arbitrary permutation at each step, and perhaps cancel some noise arising from unphysical symmetric states. However the propagation distance is governed by the Gaussian behavior of G_0, which is much shorter-ranged than the average pair separation. Hence, any cancellation would be very small. Instead, we simply use the Argonne v_8' potential in unphysical states, and include them in the propagator. In essence this corresponds to treating the particles as Boltzmann particles for purposes of the propagator. Since one always computes overlaps with completely antisymmetric states, this is perfectly acceptable.

One also has complete freedom to choose an arbitrary interaction in the unphysical channels, but the present choice retains the property of a positive definite Green's function in spin-singlet channels. The propagator in $S=0$ states is positive definite, since it is for small ϵ and the convolution form of Eq. (4.22) preserves this property. The choice of the Boltzmann propagator allows us to simply sample Gaussians centered on the identity permutation when choosing the paths.

It is also important to include many partial waves in the calculation. The starting $g_{ij}(r,r';\epsilon)$ is a narrow Gaussian of width $\sqrt{(4\hbar^2\epsilon/m)}$ which is <0.1 fm for $\epsilon < 0.1$ GeV^{-1}. Hence a large number of partial waves are required to reproduce it accurately. The propagator in all $J \le 55$ states is calculated from Eq. (4.27); beyond this we use simple approximations including the analytically known propagators for free particles. Keeping a much smaller set of partial waves would yield the same answer in an exact quadrature, however it can dramatically increase the statistical error in a Monte Carlo calculation. For example, the positive definite property described above is recovered numerically only for large numbers of partial waves.

The terms having L^2 and $(L \cdot S)^2$ operators are not presently included in the propagator. These terms, like others that depend quadratically on the relative momentum between the interacting particles, represent changes in the mass of the particles due to interactions. They can, in principle, be included by using appropriate effective masses in the kinetic energy propagator $g_{0,ij}$ [29]. Unfortunately, there is a strong spin-isospin dependence in the L^2 and $(L \cdot S)^2$ interactions, which then makes the $g_{0,ij}$ spin-isospin dependent. Attempts

to use them have generally led to large statistical errors. For this reason the propagator uses the approximate v_8' interaction operator.

Calculating this propagator is computationally intensive. Therefore, prior to the GFMC calculation, we sum the propagator over partial waves and store the full sum on a grid. Storing the $g_{JTS}^{LL'}(r,r';\Delta\tau)$ is impractical, both because of memory requirements and the fact that summing over waves for each $\mathbf{r}$ and $\mathbf{r}'$ would be computationally expensive. For a spin-independent interaction, the propagator g_{ij} would depend only upon the two magnitudes r and r' and the angle $\cos(\theta) = \hat{\mathbf{r}} \cdot \hat{\mathbf{r}}'$ between them. Here, though, there is also a dependence upon the spin quantization axis. Rotational symmetry allows one to calculate the spin-isospin components of $g_{ij}(\mathbf{r},\mathbf{r}')$ for any $\mathbf{r}$ and $\mathbf{r}'$ by simple SU3 spin rotations and values of g_{ij} on a grid of initial points $\mathbf{r}=(0,0,z)$ and final points $\mathbf{r}'=(x',0,z')$. The $x-z$ plane is chosen because the $\mathcal{Y}_{JLS}^M$ are real there. In addition, the fact that the propagator is Hermitian allows us to store only the values for $z>z'$. In the z direction we take an evenly spaced grid of 0.02 fm extending up to 6 fm. Beyond 6 fm the v_{ij} is weak and it is sufficient to use Eq. (4.15) to calculate g_{ij}. The propagator falls off approximately as a Gaussian, Eq. (4.18), with range parameter $2\hbar\sqrt{\Delta\tau/m} \sim 0.3$ fm for $\Delta\tau = 0.5$ GeV^{-1}. Thus the x' and $z-z'$ grids have maximum values of ~ 0.9 fm and are nonuniform.

C. Sampling of the paths

The remaining task in a GFMC calculation is to sample a set of paths; in order to maintain a reasonable statistical error we sum explicitly over all spin-isospin states of the system for each path. To choose the paths we follow as closely as possible the standard practice for scalar interactions, as we have done in previous work [4,8,26,29]. In this section we compare the standard method with that used for nuclear systems.

The integrals in Eq. (4.5) for $\langle \hat{O}(\tau) \rangle_{\text{Mixed}}$ are carried out stochastically using a relative probability function $P(\mathbf{P})$ to sample the paths. Each path consists of a set of n steps, where each step contains a sample of $3A$ particle coordinates, as well as sets of operator orders used to sample the symmetrization operators $\mathcal{S}$ for the pair operators in the trial wave function, Eq. (3.13), and the propagator, Eq. (4.19). The ensemble of the sampled paths is denoted by $\{\mathbf{P}\}$; and contains N_p paths. For each path $\mathbf{P}$ we define

$$N_{\mathbf{P}} = \Psi_T^\dagger(\mathbf{R}_n)\hat{O}G(\mathbf{R}_n,\mathbf{R}_{n-1})\cdots G(\mathbf{R}_1,\mathbf{R}_0)\Psi_T(\mathbf{R}_0)/P(\mathbf{P}),$$
(4.30)

$$D_{\mathbf{P}} = \Psi_T^\dagger(\mathbf{R}_n)G(\mathbf{R}_n,\mathbf{R}_{n-1})\cdots G(\mathbf{R}_1,\mathbf{R}_0)\Psi_T(\mathbf{R}_0)/P(\mathbf{P}),$$
(4.31)

and

$$\langle \hat{O}(\tau) \rangle_{\text{Mixed}} = \left(\sum_{\{\mathbf{P}\}} N_{\mathbf{P}} \right) \bigg/ \left(\sum_{\{\mathbf{P}\}} D_{\mathbf{P}} \right), \qquad (4.32)$$

with a statistical error determined by the correlated variance of $N_{\mathbf{P}}$ and $D_{\mathbf{P}}$ and proportional to $1/\sqrt{N_p}$. The relative probability function $P(\mathbf{P})$, should be chosen to minimize this statistical error.

Different schemes for sampling the paths with probability $P(\mathbf{P})$ are possible. In finite-temperature simulations, one typically retains the entire history of the path and uses a Metropolis scheme to sample them [27]. For zero-temperature simulations, however, it is generally more efficient to sample the paths through a branching random walk. Points along the path are generated iteratively through an importance-sampling procedure. Only the amplitudes of the propagated wave function and the accumulated weight of the path need be retained for each configuration. We discuss the algorithm used for nuclear spin-isospin-dependent interactions after first describing the algorithm for spin-independent interactions.

For scalar interactions and real Hamiltonians, the particles can be assigned specific spin states in $\Psi_T(\mathbf{R})$ which never change during propagation, $G(\mathbf{R}, \mathbf{R}')$ is a real, positive function with finite norm, and Ψ_T, and consequently $\Psi(\tau)$, can be chosen as a real scalar function. The $P(\mathbf{P})$ is commonly taken as

$$ P(\mathbf{P}) = \prod_{i=1,n} \left[I(\mathbf{R}_i) G(\mathbf{R}_i, \mathbf{R}_{i-1}) \frac{1}{I(\mathbf{R}_{i-1})} \right] I(\mathbf{R}_0) |\Psi_T(\mathbf{R}_0)|. $$

(4.33)

The importance function $I(\mathbf{R})$ is used in sampling and hence should be positive definite, it is often taken to be the magnitude of the trial wave function,

$$ I(\mathbf{R}) = |\Psi_T(\mathbf{R})|. $$

(4.34)

The initial configurations are sampled from $I(\mathbf{R}_0)|\Psi_T(\mathbf{R}_0)|$. The quantity in brackets in Eq. (4.33) is referred to as the importance-sampled Green's function G_I,

$$ G_I(\mathbf{R}_i, \mathbf{R}_{i-1}) = \left[I(\mathbf{R}_i) G(\mathbf{R}_i, \mathbf{R}_{i-1}) \frac{1}{I(\mathbf{R}_{i-1})} \right]. $$

(4.35)

The probability of the path $P(\mathbf{P})$ depends implicitly upon all of the steps in the path, but is decomposed into an initial weight $I(\mathbf{R}_0)|\Psi_T(\mathbf{R}_0)|$, times a product of weights for each step.

Using this $P(\mathbf{P})$ in our expressions for $N_\mathbf{P}$ and $D_\mathbf{P}$ we arrive at

$$ N_\mathbf{P} = \frac{\Psi_T(\mathbf{R}_n)\hat{O}}{I(\mathbf{R}_n)} \frac{\Psi_T(\mathbf{R}_0)}{|\Psi_T(\mathbf{R}_0)|}, $$

(4.36)

$$ D_\mathbf{P} = \frac{\Psi_T(\mathbf{R}_n)}{I(\mathbf{R}_n)} \frac{\Psi_T(\mathbf{R}_0)}{|\Psi_T(\mathbf{R}_0)|}. $$

(4.37)

In the ideal case of a Bose ground state, $\Psi_T(\mathbf{R})$ is positive for all $\mathbf{R}$; choosing $I(\mathbf{R}) = \Psi_T(\mathbf{R})$ yields $D_\mathbf{P} = 1$ with zero variance and the variance of $N_\mathbf{P}$ is acceptable for many interesting operators. In particular, if $\Psi_T(\mathbf{R})$ is close to the ground state of H, then

$$ \frac{\Psi_T(\mathbf{R})H}{\Psi_T(\mathbf{R})} \sim E_0, $$

(4.38)

and the $N_\mathbf{P}$ for $\langle H(\tau) \rangle_{\text{Mixed}}$ will have a small variance. Many properties of Bose liquid and solid ^{4}He and its drops have been studied with GFMC [27,30,31] using this probability density.

In contrast, the wave functions of simple Fermi systems have domains of positive and negative signs separated by nodal surfaces. The importance function I given in Eq. (4.34) must be increased slightly near the nodal surfaces to allow diffusion between the domains. When the path $\mathbf{P}$ crosses a nodal surface its $D_\mathbf{P}$ and $N_\mathbf{P}$ change sign. At small τ, few paths are long enough to cross nodal surfaces and the variance is small. As τ increases, many paths cross nodal surfaces, the variance increases and the average value of $D_\mathbf{P}$ decreases. This problem is called "the Fermion sign problem," and it limits the maximum value of τ up to which the state can be propagated [32,33]. Generally the calculations are continued until the statistical error increases beyond an "acceptable" point; we iterate until $\tau = 0.06$ MeV^{-1} for most nuclei studied here.

For local spin-isospin independent interactions, ^{3}H, ^{3}He, and ^{4}He nuclei would be completely spatially symmetric and no sign problem would exist. For more realistic local interactions, the dominant spatially symmetric component of the wave function and the relatively large excitation energies imply that the sign problem is not very significant for three- and four-body nuclei [34]. However, it does limit the propagation of states with $A > 4$ which must have nodal surfaces as required by antisymmetry, and also all calculations with nonlocal interactions.

Implementing the algorithm to sample the paths is straightforward. Choosing $I(\mathbf{R}) = |\Psi_T(\mathbf{R})|$, the initial ($\tau = 0$) configuration $\mathbf{R}_0$ for each path is obtained, as in VMC, by sampling $\Psi_T^2(\mathbf{R})$ using the Metropolis method. The subsequent configurations $\mathbf{R}_i$, at $\tau = i\Delta\tau$, are obtained sequentially from $\mathbf{R}_{i-1}$, by iterating with the importance-sampled Green's function G_I,

$$ I(\mathbf{R}_i)\Psi(\mathbf{R}_i) = \int G_I(\mathbf{R}_i, \mathbf{R}_{i-1}) I(\mathbf{R}_{i-1})\Psi(\mathbf{R}_{i-1}) d\mathbf{R}_{i-1}. $$

(4.39)

This equation is the importance-sampling generalization of the iterative form of Eq. (4.4),

$$ \Psi(\mathbf{R}_i) = \int G(\mathbf{R}_i, \mathbf{R}_{i-1})\Psi(\mathbf{R}_{i-1}) d\mathbf{R}_{i-1}. $$

(4.40)

Equation (4.39) describes the evolution of the density $I(\mathbf{R}_i)|\Psi(\mathbf{R}_i)|$ with $\tau = i\Delta\tau$, hence the configurations $\mathbf{R}_i$ are distributed with this density. The propagation is entirely in terms of distinguishable "Boltzmann" particles; the Fermi or Bose character of the system is retained only at the two ends of the walk through the statistics of the initial and final trial wave functions.

Up to this point, we have assumed that we can sample points along the path directly from G_I, but typically this is not possible. One must sample from an approximate $\widetilde{G}_I(\mathbf{R}_i, \mathbf{R}_{i-1})$ and then use the weighting and branching techniques discussed below to create paths with probability pro-

portional to the product of the $G_I(\mathbf{R}_i, \mathbf{R}_{i-1})$. If points are sampled from an approximate $\widetilde{G}_I$, it is convenient to define a weight

$$\widetilde{W}(\mathbf{R}_i, \mathbf{R}_{i-1}) = \frac{G_I(\mathbf{R}_i, \mathbf{R}_{i-1})}{\widetilde{G}_I(\mathbf{R}_i, \mathbf{R}_{i-1})} \tag{4.41}$$

as the ratio of the full G_I to the approximate $\widetilde{G}_I$. Simply choosing paths with $P(\mathbf{P}) = \Pi_{i=1,n} \widetilde{G}_I(\mathbf{R}_i, \mathbf{R}_{i-1}) I(\mathbf{R}_0) |\Psi_T(\mathbf{R}_0)|$ would modify expressions for the the numerator and denominator, Eqs. (4.36) and (4.37), by multiplying the contribution of each path by the product of the $\widetilde{W}$:

$$N_\mathbf{P} = W(\mathbf{P}) \frac{\Psi_T(\mathbf{R}_n) \hat{O}}{I(\mathbf{R}_n)} \frac{\Psi_T(\mathbf{R}_0)}{|\Psi_T(\mathbf{R}_0)|}, \tag{4.42}$$

$$D_\mathbf{P} = W(\mathbf{P}) \frac{\Psi_T(\mathbf{R}_n)}{I(\mathbf{R}_n)} \frac{\Psi_T(\mathbf{R}_0)}{|\Psi_T(\mathbf{R}_0)|}, \tag{4.43}$$

where

$$W(\mathbf{P}) = \prod_{i=1,n} \widetilde{W}(\mathbf{R}_i, \mathbf{R}_{i-1}). \tag{4.44}$$

As a trivial example, one could sample the free-particle propagator ($\widetilde{G}_I = G_0$), and the weights $\widetilde{W}$ would be the ratio of final to initial importance functions times the ratio of interacting to free-particle propagators. Such a scheme, however, is woefully inefficient. As the path length increases, so do the fluctuations in the $W(\mathbf{P})$, and the branching techniques discussed below must eventually be used to control them.

For an efficient and unbiased calculation, it can be very important to choose a $\widetilde{G}$ to minimize fluctuations in the weights $\widetilde{W}$ introduced at each step. For scalar problems, one typically samples a shifted Gaussian, where the shift is related to the logarithmic derivative of the trial wave function. This can be used to perform importance sampling accurate to second order in $\Delta\tau$ (for a review, see Ref. [35]), and hence essentially set $\widetilde{G}_I = G_I$.

In the nuclear case, though, the wave function consists of many spin-isospin amplitudes, and a more complex sampling scheme is required. For illustrative purposes, we describe the scalar equivalent of our sampling method, although for scalar interactions it is not as efficient as sampling a shifted Gaussian. The free propagator, $G_0(\mathbf{R}', \mathbf{R}_{i-1})$, can be easily sampled. A number of points, $\mathbf{R}'_j$, $j = 1, n_{samp}$ are obtained by sampling $G_0(\mathbf{R}'_j, \mathbf{R}_{i-1})$. These points should be chosen in a correlated manner to reduce fluctuations. Anticipating requirements for the nonscalar case, we define an approximate scalar importance-sampled Green's function $G_I^S(\mathbf{R}_i, \mathbf{R}_{i-1})$. The primary requirements are that G_I^S is fast to compute, that it is positive, and that it approximates G_I; for the scalar case one could simply choose $G_I^S = G_I$.

For each of the n_{samp} points, we calculate $G_I^S(\mathbf{R}', \mathbf{R}_{i-1})$. The $\mathbf{R}_i$ is picked from the set $\mathbf{R}'_j$ with probability proportional to $G_I^S(\mathbf{R}'_j, \mathbf{R}_{i-1}) / G_0(\mathbf{R}'_j, \mathbf{R}_{i-1})$. This procedure implicitly defines a $\widetilde{G}_I$, and requires a weight

$$\widetilde{W}(\mathbf{R}_i, \mathbf{R}_{i-1}) = \left[\frac{1}{n_{samp}} \sum_{j=1,n_{samp}} \frac{G_I^S(\mathbf{R}'_j, \mathbf{R}_{i-1})}{G_0(\mathbf{R}'_j, \mathbf{R}_{i-1})} \right] \frac{G_I(\mathbf{R}_i, \mathbf{R}_{i-1})}{G_I^S(\mathbf{R}_i, \mathbf{R}_{i-1})}. \tag{4.45}$$

Only the variance, and therefore the statistical sampling error in the calculation depends on n_{samp}. When $n_{samp} = 1$, $\mathbf{R}_i = \mathbf{R}'_1$ and the vector $\mathbf{R}_i - \mathbf{R}_{i-1}$ can be in any direction since G_0 depends only upon $(\mathbf{R}'_1 - \mathbf{R}_{i-1})^2$. In this case, the weights $\widetilde{W} = G_I / G_0$ can differ significantly from unity and add to the variance. Indeed the growth estimate of the energy, obtained from the difference between unity and the ratio of new to old weights, will have an infinite variance in the limit $\Delta\tau \to 0$. In the present calculations, we consider only two points $\mathbf{R}'_1$ and $\mathbf{R}'_2 = 2\mathbf{R}_{i-1} - \mathbf{R}'_1$ symmetric about $\mathbf{R}_{i-1}$. The leading gradient contribution along $\mathbf{R}'_1 - \mathbf{R}_{i-1}$, in the expansion:

$$\frac{G_I(\mathbf{R}'_j, \mathbf{R}_{i-1})}{G_0(\mathbf{R}'_j, \mathbf{R}_{i-1})} = 1 + (\mathbf{R}' - \mathbf{R}_{i-1}) \cdot \nabla_{\mathbf{R}'} \left(\frac{G_I(\mathbf{R}'_j, \mathbf{R}_{i-1})}{G_0(\mathbf{R}'_j, \mathbf{R}_{i-1})} \right)$$

$$+ \cdots \tag{4.46}$$

is thus cancelled up to order $\Delta\tau$ and the variations in $W(\mathbf{P})$ are reduced significantly.

Nevertheless, the weights of different paths used in computing expectation values, Eqs. (4.42) and (4.43) will eventually diverge. This divergence yields an increasing statistical error, as the contribution of only a few paths will dominate the others. Consequently, branching techniques are required to control the fluctuations in the relative contributions of different paths. In branching, the configurations are redistributed every few time steps by keeping $n_\mathbf{R}^i$ unit weight copies of each configuration where

$$n_\mathbf{R}^i = \text{int}[W(\mathbf{P}) + \zeta_\mathbf{R}], \tag{4.47}$$

$\zeta_\mathbf{R}$ is a random number between 0 and 1, and int denotes the (truncated) integer part. The $W(\mathbf{P})$ of the resulting configurations are then set to one in order to account for the branching process. This branching technique, in effect, forces the paths to be sampled from the product of G_I rather than $\widetilde{G}_I$.

On average, the expectation value of any path is reproduced correctly using this technique. However, the computation is much more efficient as configurations with small weights are more likely be discarded while configurations with large weights are replicated. In this way, statistical noise is reduced by keeping an adequate population of contributing configurations.

The algorithm used for nuclear GFMC, in which there is a strong spin-isospin dependence to the interaction, is a generalization of the procedure described above. Here wave functions must be regarded as vectors in spin-isospin space and the $G(\mathbf{R}, \mathbf{R}')$ as a matrix, however, the relative probability of the paths $P(\mathbf{P})$ must remain a scalar. Following Refs. [26,8,29], we define an importance-sampled Green's function G_I as well as an approximate $\widetilde{G}_I$. Just as in the scalar case, the approximate $\widetilde{G}_I$ is used for sampling points in the path, while the ratios $G_I / \widetilde{G}_I$ define weights $\widetilde{W}$ which are used in branching.

In order to introduce importance sampling, we first define a scalar function I of the trial and GFMC, Eq. (4.4), wave functions:

$$I[\Psi_T(\mathbf{R}_i),\Psi_i(\mathbf{P}_i)] = \left| \sum_\alpha \Psi_{T,\alpha}^\dagger(\mathbf{R}_i)\Psi_{i,\alpha}(\mathbf{P}_i) \right|$$
$$+ \epsilon \sum_\alpha |\Psi_{T,\alpha}^\dagger(\mathbf{R}_i)\Psi_{i,\alpha}(\mathbf{P}_i)|,$$
$$(4.48)$$

where Ψ_T is the trial wave function, Ψ_i is the ith iteration of the GFMC wave function, which depends implicitly upon the path $\mathbf{P}_i$, and α denotes the spin-isospin components.

This definition of the importance function differs slightly from the scalar case, which only involved the trial function Ψ_T. The first term simply measures the magnitude of the overlap of the wave functions, while the second, with a small coefficient ϵ (≈ 0.01) ensures a positive definite importance function to allow diffusion across nodal surfaces. In this definition of I as well as the remaining discussion, we suppress the sampling of the pair orders in the wave function and the propagator.

The importance-sampled Green's function G_I can then be defined as the ratio of the importance functions after one iteration of the full propagator $G(\mathbf{R}_i,\mathbf{R}_{i-1})$,

$$G_I(\mathbf{R}_i,\mathbf{R}_{i-1}) = \frac{I[\Psi_T(\mathbf{R}_i),\Psi_i(\mathbf{R}_i)]}{I[\Psi_T(\mathbf{R}_{i-1}),\Psi_{i-1}(\mathbf{R}_{i-1})]}, \quad (4.49)$$

where

$$\Psi_i(\mathbf{R}_i) = G(\mathbf{R}_i,\mathbf{R}_{i-1})\Psi_{i-1}(\mathbf{R}_{i-1}). \quad (4.50)$$

For scalar interactions, this definition of G_I is equivalent to Eq. (4.35). Here, the importance function is defined from all the amplitudes of the trial and GFMC wave functions, and the effects of the propagator are included in the importance function.

To perform a calculation, the initial configurations are sampled from $I(\mathbf{P}_0)$, which is defined by inserting $\Psi_{i=0} = \Psi_T$ in Eq. (4.48) above. For speed, the VMC calculations use the simple importance function $W_{pq}(\mathbf{R})$ defined in Eq. (3.25). Hence we introduce the ratio of the two importance functions as an initial weight and perform a branching step immediately. This procedure results in a population drawn from $I(\mathbf{P}_0)$.

Sampling steps from G_I gives us

$$P(\mathbf{P}) = \prod_{i=1,n} \frac{I[\Psi_T(\mathbf{R_i}),\Psi_i(\mathbf{R_i})]}{I[\Psi_T(\mathbf{R_{i-1}}),\Psi_{i-1}(\mathbf{R_{i-1}})]} I[\Psi_T(\mathbf{R}_0),\Psi_i(\mathbf{R}_0)]$$
$$(4.51)$$

$$= I[\Psi_T(\mathbf{R_n}),\Psi_n(\mathbf{R}_n)], \quad (4.52)$$

and hence estimates of observables as the ratio N/D where

$$N_P = \frac{\Psi_T^\dagger(\mathbf{R}_n)O\Pi_{i=1,n}G(\mathbf{R}_i,\mathbf{R}_{i-1})\Psi_0(\mathbf{R}_0)}{I[\Psi_T(\mathbf{R_n}),\Psi_n(\mathbf{R}_n)]},$$

$$D_P = \frac{\Psi_T^\dagger(\mathbf{R}_n)\Pi_{i=1,n}G(\mathbf{R}_i,\mathbf{R}_{i-1})\Psi_0(\mathbf{R}_0)}{I[\Psi_T(\mathbf{R_n}),\Psi_n(\mathbf{R}_n)]}. \quad (4.53)$$

For scalar interactions, setting $\epsilon = 0$ in the definition of I, Eq. (4.48), we recover Eqs. (4.36) and (4.37).

Again, though, we cannot sample from G_I directly. We must sample from a $\widetilde{G}_I$ and introduce weights and branching to correctly get paths sampled from the products of G_I. The procedure is exactly as described previously, although here it is important to introduce an approximate G_I^S. The G_I^S is a spin-independent function, and hence is much easier to compute than G_I, which involves all the spin-isospin states of the system. The present algorithm requires us to compute only a single full propagator per iteration, and the full trial wave function only after several iterations.

The scalar importance function $G_I^S(\mathbf{R}',\mathbf{R}_{i-1})$ is again used to implicitly define $\widetilde{G}_I$, and construct weights $\widetilde{W}_I(\mathbf{R}_i,\mathbf{R}_{i-1})$. It contains scalar approximations to the dominant physics present in the propagator and the trial wave function,

$$G_I^S(\mathbf{R},\mathbf{R}') = |\Psi_J(\mathbf{R})|G^S(\mathbf{R},\mathbf{R}')\frac{1}{|\Psi_J(\mathbf{R}')|}, \quad (4.54)$$

where $G^S(\mathbf{R},\mathbf{R}')$ is obtained from an approximate spin-isospin independent interaction:

$$v_S(r_{ij}) = \frac{1}{2}[v_c(^1S_0,r_{ij}) + v_c(^3S_1,r_{ij})] \quad (4.55)$$

and the Feynman approximation

$$G^S(\mathbf{R},\mathbf{R}') = \exp\left(-\sum_{i<j} v_S(r_{ij})\Delta\tau/2\right)$$
$$\times G_0(\mathbf{R},\mathbf{R}')\exp\left(-\sum_{i<j} v_S(r'_{ij})\Delta\tau/2\right).$$
$$(4.56)$$

This propagator uses the average of the central potentials in the important S waves, and, like the true $G(\mathbf{R},\mathbf{R}')$, is small at small r_{ij}, preventing the configurations from having small interparticle distances inside the repulsive core range. Similarly, the approximate importance sampling in G_I^S is governed by the function $|\Psi_J|$, Eq. (3.4), which can be used as a simple approximation to $|\Psi_T|$.

With these definitions, a step in the propagation is the same as in the scalar case. It begins with sampling n_{samp} correlated points $\mathbf{R}'_j$ from the free-particle propagator. Then G_I^S is evaluated for each possible step, and we choose $\mathbf{R}_i$ from them. The weight $\widetilde{W}$ is then computed as the ratio of importance functions divided by the sampling probability $\widetilde{G}$ as in Eq. (4.45).

Since we typically do not compute observables after each step, and fluctuations in the weights are not significant after a single step, it is not necessary to compute the importance function I (and hence the trial wave function) at every step. We perform branching after every second step, with the weights computed from the product of intermediate $\widetilde{W}$. This product involves only the G_I^S and overlaps of the wave functions at the final and initial steps. Hence, for intermediate steps we must compute the full G acting on the GFMC wave

function, but not necessarily the full trial wave function. Again, after branching, the weight of each path is set to $W(\mathbf{P}) = 1$.

At this point we can reconstruct the estimates of any observables. After branching, the $N_\mathbf{P}$ and $D_\mathbf{P}$ obtained with this $P(\mathbf{P})$ are given by Eq. (4.53). Ignoring ϵ, the variance of $D_\mathbf{P}$ is mostly due to the fermion sign problem, while that of $N_\mathbf{P}$ is tolerable, particularly when $\hat{O} = H$ and Ψ_T is close to the desired eigenfunction of H. For an exact Ψ_T, we regain the exact ground-state energy with zero variance.

V. COMPUTATIONAL METHODS

The complicated nature of the nuclear interaction and the computational complexity of the calculations presented here require high performance computing. In the past, vector supercomputers were used for the first ^{4}He and ^{5}He GFMC calculations. As we have stated before, the size of the wave-function vector grows exponentially with the number of nucleons and the number of matrix operations grows with the number of pairs. In making the step from four- to six-body calculations at least an order of magnitude increase in computational performance was required. The clear means of achieving this performance goal was parallel computation.

A frequent method of achieving performance gains in Monte Carlo calculations is to distribute the configurations over several processors and let each processor carry out its own independent Monte Carlo calculation. Such an ''embarrassingly parallel'' implementation is sufficient for simple calculations in which each processor can handle a calculation with a minimum acceptable number of configurations in a reasonable amount of time. For the seven-body systems considered here this is not the case.

The heart of the VMC calculation is the Metropolis algorithm which is an inherently serial algorithm. Since the bulk of the work in our variational calculations lies in the energy expectation value, the straightforward division of labor is to have one master processor perform the Metropolis walk, while several slave processors calculate the energy and other expectation values for the configurations that the master generates. The number of slave processors that can be efficiently used is the ratio of the CPU time needed for expectation values to that needed to walk from one configuration to the next. We find that typically 50 processors can be used efficiently in a ^{7}Li VMC calculation.

Implementing the GFMC algorithm on a parallel architecture provides some special challenges. There is no clear division of labor as in the VMC calculation and the number of configurations can change throughout the calculation. An embarrassingly parallel implementation could work for ^{6}Li, since one processor on current machines is capable of handling enough ^{6}Li configurations (several thousands) for an independent GFMC calculation. For ^{7}Li, on the other hand, only hundreds of configurations could be propagated on each processor to achieve an acceptable turnaround time for an independent calculation. With such a small configuration set on each node, the population fluctuations on each processor would leave some processors with few configurations and others with too many. To avoid such an inefficient use of resources, periodic load balancing between processors is required.

In our implementation, the initial configurations are generated and written to disk in a random walk that uses only two processors. Typically 50 000 configurations are generated. These are then used in one or more subsequent GFMC calculations. At the start of the GFMC calculation, the master processor reads the configurations and distributes them to the slave processors. It is then responsible for collecting and averaging energy expectation values, and determining load-balancing distributions. Each of the slave processors is responsible for a block of configurations. The slaves perform propagation and branching for this block of configurations. At selected values of τ (typically every 20 steps) they save the configurations in local lists for subsequent energy calculations. During load balancing (which typically is done every 10 steps) each slave reports its current load to the master, which then instructs each overloaded slave to send its excess configurations to underloaded slaves. In this way, all slaves have, within tolerances, the same number of configurations. The master must receive load information from all the slaves before it can determine the redistribution. In order that slaves not remain idle while waiting for the redistribution information, they compute energies for the configurations stored in their local lists. When a slave completes a block of energy calculations for a particular time step, they are sent back to the master. After all of the energy results for a time step are received by the master, they are averaged. This program structure scales well with the number of processors since there are no major communication bottlenecks in the course of the calculation and load balancing keeps the slaves somewhat synchronized. Calculations with up to 50 processors on the Argonne IBM SP show no degradation in efficiency; typically the slaves are idle less than 5% of the time and most of this idle time occurs at the end of the calculation.

The current version of our GFMC program is written using FORTRAN 90 and makes use of the MPI message-passing library. On IBM SP1 processors, we achieve 40% (33%) of the theoretical speed in ^{6}Li (^{7}Li) calculations. On IBM SP2 wide nodes we get 45% for both cases. The better efficiency can be ascribed to the larger cache on the wide nodes. Table VIII shows the performance of our GFMC program on the Argonne IBM SP (using SP1 nodes) and the Cornell IBM SP2 using wide nodes. The table gives the CPU times for a single propagation step and a single energy evaluation and the total time required for 50 000 configurations propagated for 120 time steps ($\Delta\tau = 0.0005$ MeV^{-1}, $\tau_{\text{final}} = 0.06$ MeV^{-1}) with load balancing every 10 time steps and energy evaluations every 20 steps; this time includes slave idle time and average effects of configuration number growth. It is based on results using 20–40 slaves. However, this total time does not include the master time. As one can see, the time grows by roughly a factor of 10 from ^{4}He to ^{6}Li to ^{7}Li. The total computational effort approximately scales as the product of the wave function size $N(A,T) = 2^A \times I(A,T)$ [Eq. (3.28)] and the number of pairs $P = \frac{1}{2}A(A-1)$. This rapid increase in computation time will be a serious obstacle to extending these calculations beyond eight-body nuclei on presently available computers.

Our earlier six-body calculations [4] were about 30 times slower than those we now make. The increased speed is approximately attributable to (1) using the exact two-body

TABLE VIII. GFMC program performance on IBM SP1 and SP2 Wide Nodes. $N(A,T)$ is the number of spin-isospin states in the wave function and P is the number of pairs. The columns give the times for one propagation step and one energy evaluation and the total time needed for a 50 000 configuration calculation; see the text for a more complete description.

			Propagation msec		Energy calculation sec		Total node hours	
	$N(A,T)$	P	SP1	SP2	SP1	SP2	SP1	SP2
^{4}He	32	6	6.6	3.4	0.025	0.01	13	7
$A=6;T=0$	320	15	63	26	0.84	0.31	220	80
$A=6;T=1$	576	15	100	40	1.66	0.56	290	125
$A=7;T=\frac{1}{2},\frac{3}{2}$	1792	21	460	170	10.6	3.4	2230	725

propagator (factor of 3), (2) dropping the $\epsilon_C V_{ijk}^C$ term in the Ψ_T (factor 2), (3) improvements in the calculation of the wave functions (factor 3), and (4) reduction of processor idle time (factor 1.4).

VI. ACCURACY OF GFMC

In this section we consider several aspects of our calculations that could introduce systematic errors in the GFMC results, and attempt to place limits on these errors. There are two major sources of error: due to the fermion sign problem, the GFMC propagation cannot be extended to arbitrary large imaginary time and thus admixtures of low-energy excitations in the trial wave function will not be fully removed, and the GFMC propagation must be done with a different Hamiltonian from the desired one. We also investigate the effects of the time step size.

Figure 3 shows the statistical errors as a function of imaginary time for calculations of $\langle H \rangle$ for various nuclei using 50 000 initial configurations. The errors grow dramatically with increasing A due to the increasingly poorer quality of the Ψ_T. In these calculations, $\langle \Psi_T | H | \Psi(\tau) \rangle$ is evaluated by having H act entirely to the left, therefore if Ψ_T is an eigenfunction of H, the sampling errors will be nil as per Eq. (4.5). For the p-shell nuclei, the errors increase exponentially

with τ. This is the well-known fermion sign problem; the s-shell nuclei suffer much less from this problem [34]. This exponential error growth places an effective limit of $\tau_{final}=0.06$ MeV^{-1} on our calculations for $A=7$ nuclei, which means that admixtures of states of excitation energy less than ~ 12 MeV in Ψ_T, will be damped by less than 50%.

This led us in Ref. [4] to attempt to extrapolate the computed $E(\tau)$ to $\tau=\infty$ by fitting them with

$$E(\tau)=E_0+\frac{\sum_i \alpha_i^2 E_i^\star \exp(-E_i^\star \tau)}{1+\sum_i \alpha_i^2 \exp(-E_i^\star \tau)}, \qquad (6.1)$$

where E_0 is the extrapolated energy, and the strengths of contaminating states in Ψ_T are approximated with a few α_i^2 at excitation energies $E_i^\star$. Figure 4 shows such fits made for ^{4}He. Because ^{4}He calculations are so inexpensive, we were able to make precise calculations of $E(\tau)$ for many values of τ and thus determine the short-time behavior of $E(\tau)$ using 200 000 to 740 000 configurations. The solid curve is a fit with $E_0=-28.335$ MeV, excitation energies $E_i^\star=20.2, 341$, and 1477 MeV, and corresponding $\alpha_i^2=0.0062, 0.0018$, and
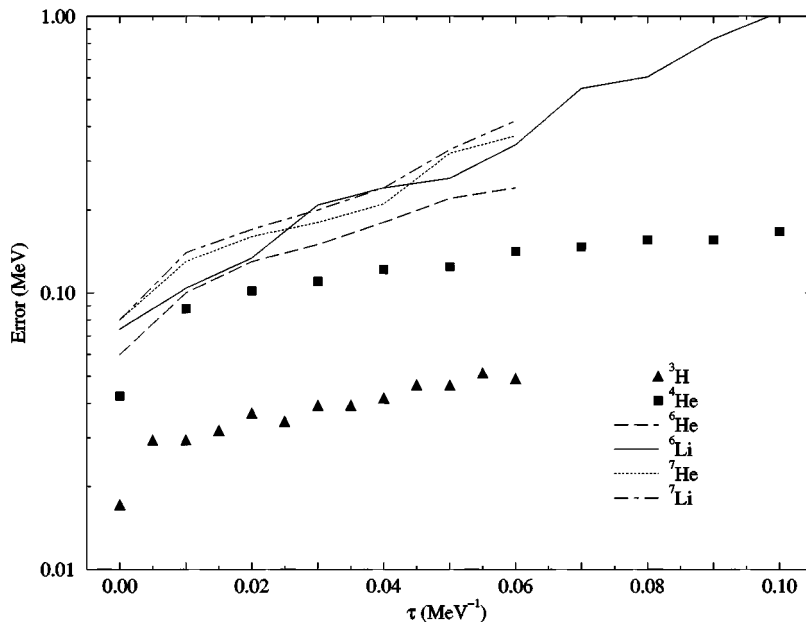

FIG. 3. Statistical errors (MeV) in GFMC calculations with 50 000 initial configurations as a function of imaginary time.

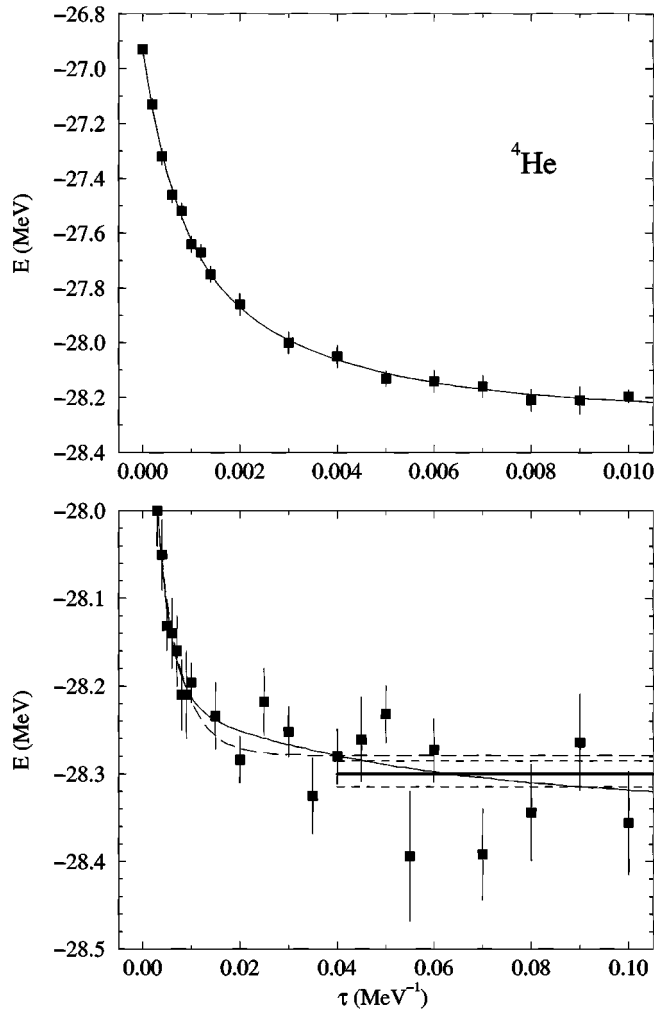FIG. 4. ^{4}He GFMC energy as a function of imaginary time. The fits are described in the text.

FIG. 5. ^{6}Li GFMC energy as a function of imaginary time. The fits are described in the text.

0.000 46. The lowest 0^+ excitation of ^{4}He is at 20.2 MeV and this energy was not varied in the fit. The χ^2 of the fit is 19 for 31 $E(\tau)$ (25 degrees of freedom), so the $E(\tau)$ are not statistically independent. We have not attempted to estimate the correlations between the energies at different times. The χ^2 increases by 1 when E_0 is changed by $+0.02$ or -0.03. The dashed curve shows a fit without the 20.2 MeV excitation; it gives $\chi^2 = 23$ and $E_0 = -28.28$ MeV. For most of the other GFMC calculations reported in this paper, we did not compute $E(\tau)$ at the many $\tau < 0.1$ MeV^{-1} used in these fits. Therefore we made several fits to the $E(\tau)$ for $\tau \geqslant 0.1$. A fit using $E_1^\star = 20.2$ MeV and one adjustable $E_i^\star$ gives $E_0 = -28.33(3)$ with $\chi^2 = 14.6$ (11 degrees of freedom), while a fit with just one $E_i^\star$ results in $E_0 = -28.33^{+0.04}_{-0.12}$, $E_1^\star = 30$, and $\chi^2 = 16.0$. Finally, the heavy solid line with short dashed error bars shows the average of the $E(\tau)$ for $0.04 \leqslant \tau \leqslant 0.1$: $-28.300(15)$. It appears that in this most favorable case, with high statistics, high first excited state, and large maximum τ, we can see that including the first excited state improves the extrapolation marginally. However, the extrapolated E_0 is not significantly lower than a simple average of the $E(\tau)$ for $0.04 \leqslant \tau \leqslant 0.1$.

Figure 5 shows the $E(\tau)$ and fits made for the ground state of ^{6}Li. The values for $\tau > 0.06$ MeV^{-1} were computed with 200 000 initial configurations, those for $\tau = 0, 0.01, \ldots, 0.06$ MeV^{-1} have 280 000 configurations, while those for the other small τ have only 50 000 configurations. The energy at very small τ is influenced by admixtures of very high-energy states in Ψ_T. These have little effect on the $E(\tau > 0.1$ MeV$^{-1})$, therefore we make fits to $E(\tau)$ only for $\tau > 0.01$. The dashed curve is a fit to the $E(\tau)$ for $0.01 \leqslant \tau \leqslant 0.06$, which is the range that is available for the other p-shell nuclear states in this paper. The extrapolated energy is $E_0 = -31.56^{+0.24}_{-0.50}$ MeV, where the indicated errors correspond to χ^2 increasing by 1. This fit was made using a single excitation energy, $E_1^\star = 36$ MeV. The first 1^+ excited state of ^{6}Li is at 5.65 MeV. A single-energy fit constrained to this energy gives large χ^2. Two-energy fits with one energy constrained to 5.65 MeV have a very flat $\chi^2(E_0)$ from which useful values of E_0 cannot be extracted. The solid curve shows a single-energy fit made to the $E(\tau)$ up to 0.1 MeV^{-1} available for this state; it gives $E_0 = -31.38^{+0.12}_{-0.18}$. We see that including data up to 0.1 MeV^{-1} reduces the error in E_0 by about a factor of 2. Finally the solid line with short dashed error bars is the average of the $\tau = 0.04, 0.05,$ and 0.06 values, denoted by E_{av}. Its value, $-31.25(11)$ MeV, is formally an upper bound for E_0 and is above the extrapolated E_0 by only one standard deviation.

Because of the difficulties in making useful extrapolations in τ, it is important to understand contaminations in Ψ_T, particularly from low-excitation-energy states which will not be fully filtered out by $\tau = 0.06$ MeV^{-1}. We have made several calculations of the ground state of ^{6}Li to study the effects of changes in Ψ_T on the GFMC $E(\tau)$. Figure 6 shows the effects of removing some of the noncentral correlations in Ψ_T; the solid circles are from a calculation with the full Ψ_T and are the same as in Fig. 5. The open diamonds were computed by using the simpler Ψ_P of Eq. (3.3). This makes the energy at $\tau = 0$ worse by ~ 1.7 MeV. However by $\tau = 0.01$, the GFMC has fully corrected for this defect and thereafter the differences are just statistical fluctuations. Hence removing $\widetilde{U}_{ijk}^{\text{TNI}}$ from Ψ_T enhances the admixtures of excitations > 250 MeV. Calculations without the $\widetilde{U}_{ijk}^{\text{TNI}}$ would be about 20% faster than full calculations, but the poorer
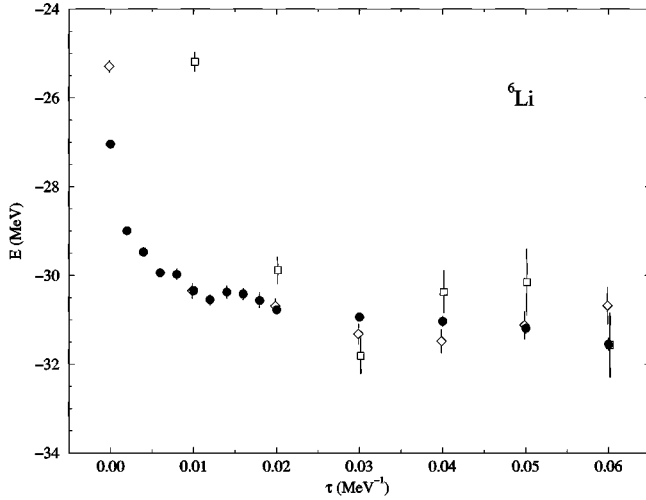
FIG. 6. ^{6}Li GFMC energy as a function of imaginary time for various truncations of the noncentral parts of Ψ_T.

FIG. 7. ^{6}He GFMC energy as a function of imaginary time for Ψ_T with various one-body Φ.

quality of Ψ_T without $\widetilde{U}_{ijk}^{\rm TNI}$ increases the statistical errors at large τ by about 20%, and thus requires 40% more configurations to get the same error. Therefore it is not economical to drop the $\widetilde{U}_{ijk}^{\rm TNI}$ from Ψ_T.

The open squares in Fig. 6 come from a much more drastic approximation of Ψ_T. Here both the $\widetilde{U}_{ijk}^{\rm TNI}$ and tensor components U_{ij} have been omitted, resulting in a four-operator wave function. In such a wave function, the dominant tensor components of the two-body potential have zero expectation value and the energy at $\tau=0$ is $+41$ MeV. It is completely corrected by $\tau=0.03$; again the rate of correction indicates excitation energies ~ 250 MeV. The statistical errors from such a bad Ψ_T are much larger.

These two tests indicate that defects in the noncentral parts of the correlation, which have been the subject of much optimization in VMC studies, are easily corrected by the GFMC. Deficiencies in the one-body part of Ψ_T present more of a problem. As is discussed in Sec. III, the Ψ for ^{6}He has two symmetry components: [2] and [11]; the optimal amplitudes for these (see Table VI) are 0.967 and -0.253, respectively. The solid circles in Fig. 7 show GFMC energies from a Ψ_T using these components. The open squares show results computed using a Ψ_T with just the [11] component; the $E(\tau=0)$ obtained with such a wave function is 4.5 MeV higher than that obtained with the best Ψ_T; this corresponds to the 5 MeV excitation energy of the dominantly [11] state. However, because this error is entirely due to a low-energy excitation, the GFMC makes very little improvement by $\tau=0.05$ MeV^{-1}. A less radical case is shown by the open diamonds which correspond to a Ψ_T with amplitudes of $+1/\sqrt{2}$, $-1/\sqrt{2}$ for the two states. The $E(\tau)$ starts out 1.6 MeV above that of the best Ψ_T; the GFMC reduces this to ~ 1.3 MeV at $\tau=0.06$ MeV^{-1}. The solid curve is a single-energy fit to these results; the fitted excitation energy is 36 MeV and the extrapolated $E_0=-26.7$ is well above the $E_{\rm av}=-27.64(14)$ from the best Ψ_T. Fits with two excitations, one constrained to 5.0 MeV, give an essentially flat χ^2, and are not useful to extract the E_0.

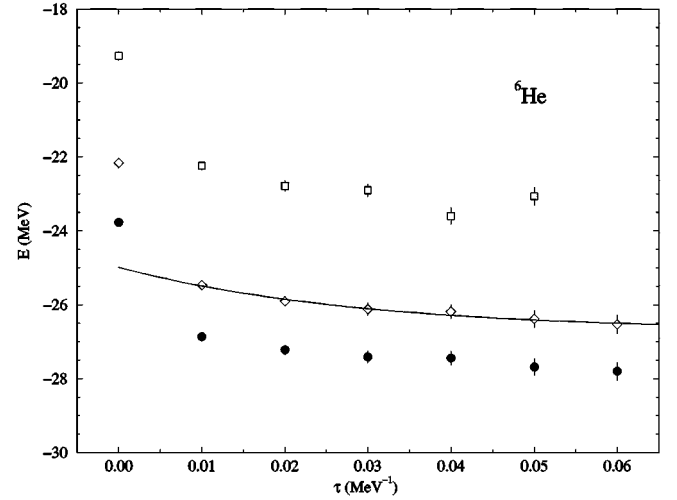A similar situation arose in our first GFMC calculation for the ground state of ^{7}He. This was made with just the dominant $^2P[21]$ component. A subsequent calculation using the three components listed in Table VII lowered all the $E(\tau)$ by ~ 0.8 MeV; the first $\frac{3}{2}^-$ excited state is at only 2 MeV so we would have to propagate 10 times further for the GFMC to substantially correct this error.

It is important that the Ψ_T have the correct admixtures of different symmetry, and other low-lying states. Otherwise the GFMC results will only be upper bounds to the exact eigenenergies. For this reason the Ψ_T used in this work are obtained by diagonalizing the Hamiltonian in the small bases of low-energy shell-model states as discussed in Sec. IV. Such diagonalizations can be used to ascertain if an improved Ψ_T' will influence the GFMC results obtained with Ψ_T. The Hamiltonian should be diagonalized between Ψ_T' and Ψ_T, taking into account their nonorthogonality. If the difference in the eigenvalues is large compared to $1/\tau_{\rm final}$ the results will not be influenced; if it is small, the superposition corresponding to the lowest eigenvalue must be used. As examples of this, we made such diagonalizations for the cases studied above, in which Ψ_P or just a four-operator Ψ_P were used. These gave excitation energies of ~ 700 and ~ 300 MeV, respectively, which are in good agreement with the observed $E(\tau)$. Our best Ψ_V contains U_{ij}^{LS} and U_{ijk} correlations omitted from the Ψ_T due to computational costs. Diagonalizing the Hamiltonian within Ψ_V and Ψ_T shows that these correlations admix states with excitation energies of ~ 1000 and 300 MeV, respectively. Thus they can be safely left out of the Ψ_T.

As is discussed in Sec. III, the VMC calculations for p-shell nuclei do not have a local variational minimum for reasonable rms radii. Therefore the variational searches were constrained to have radii close to the experimental values, if such values are known. To study the sensitivity of the GFMC results to this assumption, we have made a number of GFMC calculations of the ^{6}Li ground state using Ψ_T that have different rms radii. These Ψ_T were made by changing the depth (V_p) and radius (R_p) of the Woods-Saxon well used to make the p-wave orbitals [see Eq. (3.19)]; thus the ^{4}He core was not directly modified. Figure 8 shows the evolution of the rms radius with τ for these calculations; the solid circles
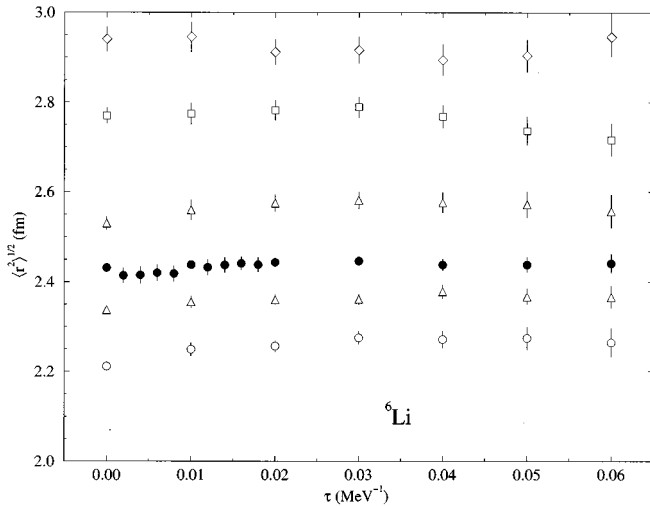
FIG. 8. ^{6}Li rms radii as a function of imaginary time for GFMC calculations with Ψ_T of varying rms radii.

correspond to the Ψ_T used in the rest of this paper. We see that the GFMC basically makes no change to the radii, even though they span a range of almost 30% (there may be some indication that the smallest radii are increased at small τ). This is probably because completely separating the deuteron from the ^{4}He core corresponds to only a 1.5 MeV excitation. Figure 9 shows the GFMC energies from these calculations as a function of the GFMC radii (both are averages of the $0.04 \leqslant \tau \leqslant 0.06$ MeV^{-1} values), and the corresponding Ψ_T expectation values. The variational energies obtained with Ψ_T decrease monotonically with increasing rms radius, but the GFMC energies show a weak minimum; the very large radii yield higher GFMC energies and thus can be variationally ruled out. The curve is a parabolic fit to the five GFMC energies with smallest rms radii; the minimum is at 2.44 fm. However the curve is very flat and the uncertainty in the location of the minimum is at least 0.1 fm. Thus even when 50 000 to 280 000 initial configurations are used for each
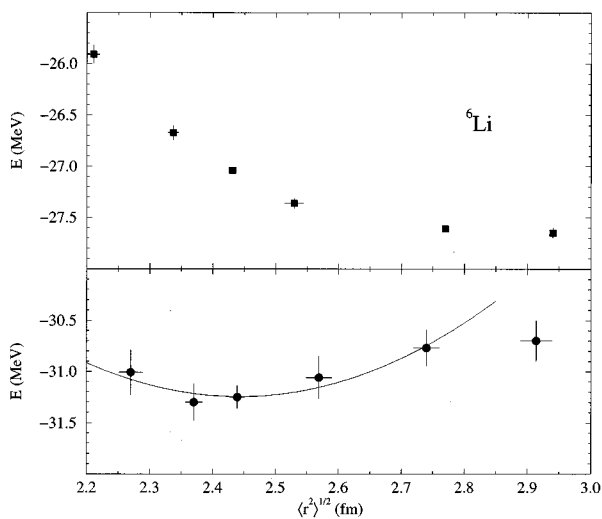
FIG. 9. ^{6}Li VMC (above) and GFMC (below) energies versus the rms radii from calculations with Ψ_T of varying rms radii.

point, it is difficult to extract the ^{6}Li rms radius. Given this, it is not possible at present to reliably study the radii of $A=7$ nuclei.

The GFMC propagator used in these calculations has two possible sources of error. The first is that the time step, $\Delta\tau=0.0005$ MeV^{-1}, might be too large. We have checked this by two calculations. For ^{3}H we made calculations to $\tau=0.06$ MeV^{-1} using both $\Delta\tau=0.0005$ and $0.000\,25$ MeV^{-1}; these were different by 0.016(14) MeV. For ^{4}He we made calculations to $\tau=0.01$ MeV^{-1} using both $\Delta\tau=0.0005$ and 0.0001 MeV^{-1}; these were different by 0.02(6) MeV. The statistical errors in our GFMC energies for p-shell nuclei are all >0.1 MeV; thus these time-step effects are negligible.

The second possible source is that we cannot use a propagator for the full Hamiltonian, H, that we are interested in. Rather we must use the H' of Eq. (2.17) and compute $\langle H - H' \rangle$ perturbatively. Kamada and Glöckle [36] have estimated for ^{3}H that evaluating $\langle v_{ij} \rangle$ in wave functions appropriate for v'_{ij} underestimates the binding energy by <20 keV; scaling this by the total two-body potential energy gives <50 keV in ^{4}He and <90 keV in ^{7}Li. We constructed a ^{4}He Ψ_V that is optimized for $v'_{ij}+V_{ijk}$ and used it to compute $\langle v_{ij} \rangle$; this gives 60(15) keV less binding than our best ^{4}He variational wave function in agreement with the above estimates.

Using a propagator for an H' that gives more binding than H can introduce small errors in the determination of densities and radii. The more tightly bound eigenstate of H' is likely to have a smaller radius. The radii of ^{4}He can be calculated more accurately, and we have studied their sensitivity to various propagators. The rms radius for Ψ_T optimized for H is 1.482(3) fm. A GFMC calculation using an H' with no $v'_C(r_{ij})$ and $V'_{ijk}=V_{ijk}$ [see Eq. (2.17)] gives $\langle H-H' \rangle=2.40(3)$ MeV and an rms radius of 1.418(4). However using the $v'_C(r_{ij})$ and $1.3U_0$ in V'_{ijk} results in $\langle H-H' \rangle=0.03(2)$ MeV and an rms radius of 1.446(3) fm. Presumably the later value is more correct, while the former is too small due to the overbinding.

As is discussed in Sec. IV, the GFMC directly computes mixed estimates $\langle O(\tau) \rangle_{\text{Mixed}}$. Except for H' and operators that commute with it, these must be corrected to obtain the desired $\langle O(\tau) \rangle$; we use Eq. (4.8) to achieve this. Consequently, the expectation values of the individual energy components, such as K^{Cl}, v'_{ij}, and V'_{ijk}, which have errors of the order $|\Psi_0-\Psi_T|^2$, do not sum to the correct total energy. Indeed, there must be a collective error in these individual terms equal to the total difference between the GFMC $\langle H' \rangle_{\text{Mixed}}$ and the VMC $\langle H' \rangle_T$. This is illustrated in Table IX for the case of ^{6}Li, where the difference $\langle H' \rangle_{\text{Mixed}}-\langle H' \rangle_T$ is -4.4 MeV, and the sum of the individual $\langle O \rangle$ is an additional -4.4 MeV lower than $\langle H' \rangle$. In this case, the individual corrections are comparable in magnitude to the collective error, but small compared to the total expectation values.

Aside from our own work in Ref. [4], there are no published calculations of p-shell nuclei using realistic interactions such as those used here, to our knowledge. However we can compare to previous values for the s-shell nuclei. There are accurate Faddeev and projected hyperspherical

TABLE IX. Contributions to the GFMC $\langle O(\tau) \rangle$ of Eq. (4.8) for ^{6}Li. All quantities are in MeV.

	$\langle O \rangle_T$	$\langle O \rangle_{\text{Mixed}}$	$\langle O \rangle_{\text{Mixed}} - \langle O \rangle_T$	$\langle O \rangle$
K^{CI}	143.8(4)	147.3(5)	3.5(7)	150.8(10)
v'_8	$-168.7(4)$	$-175.7(6)$	$-7.0(8)$	$-182.6(11)$
v'_C	1.5(0)	1.5(0)	0.0(0)	1.5(0)
V_{ijk}	$-3.5(1)$	$-4.4(1)$	$-0.9(1)$	$-5.4(1)$
Sum	$-26.9(1)$	$-31.3(1)$	$-4.4(1)$	$-35.7(1)$
H'	$-26.9(1)$	$-31.3(1)$		$-31.3(1)$

TABLE X. Experimental and quantum Monte Carlo energies of $A = 2-7$ nuclei in MeV.

$^AZ(J^\pi;T)$	VMC (Ψ_T)	VMC (Ψ_V)	GFMC	Expt.
^{2}H(1^+;0)	$-2.2248(5)$			-2.2246
^{3}H($\frac{1}{2}^+;\frac{1}{2}$)	$-8.15(1)$	$-8.32(1)$	$-8.47(1)$	-8.48
^{4}He(0^+;0)	$-26.93(2)$	$-27.78(3)$	$-28.30(2)$	-28.30
^{6}He(0^+;1)	$-23.77(6)$	$-24.87(7)$	$-27.64(14)$	-29.27
^{6}He(2^+;1)	$-22.05(6)$	$-23.01(7)$	$-25.84(11)$	-27.47
^{6}Li(1^+;0)	$-27.04(3)$	$-28.09(7)$	$-31.25(11)$	-31.99
^{6}Li(3^+;0)	$-23.98(7)$	$-25.16(7)$	$-28.53(32)$	-29.80
^{6}Li(0^+;1)	$-23.18(6)$	$-24.25(7)$	$-27.31(15)$	-28.43
^{6}Li(2^+;0)	$-22.58(10)$	$-23.86(8)$	$-26.82(35)$	-27.68
^{6}Be(0^+;1)	$-21.73(6)$	$-22.79(7)$	$-25.52(11)$	-26.92
^{7}He($\frac{3}{2}^-;\frac{3}{2}$)	$-19.02(8)$	$-20.43(12)$	$-25.16(16)$	-28.82
^{7}Li($\frac{3}{2}^-;\frac{1}{2}$)	$-31.59(8)$	$-32.78(11)$	$-37.44(28)$	-39.24
^{7}Li($\frac{1}{2}^-;\frac{1}{2}$)	$-31.13(8)$	$-32.45(11)$	$-36.68(30)$	-38.76
^{7}Li($\frac{7}{2}^-;\frac{1}{2}$)	$-25.77(6)$	$-27.30(11)$	$-31.72(30)$	-34.61
^{7}Li($\frac{5}{2}^-;\frac{1}{2}$)	$-24.91(7)$	$-26.14(11)$	$-30.88(35)$	-32.56
^{7}Li($\frac{3}{2}^-;\frac{3}{2}$)	$-18.27(7)$	$-19.73(12)$	$-24.79(18)$	-28.00

harmonics (PHH) calculations of ^{3}H for the Argonne v_{14} with no V_{ijk}. For this Hamiltonian we find a GFMC energy of $-7.670(8)$ MeV which is in good agreement with the previous results of -7.670 (Faddeev/R [37]), -7.680 (Faddeev/Q [38]), and -7.683 (PHH [39]). A PHH result for Argonne v_{18} with Urbana IX has recently been computed [40]: -8.475. It is in good agreement with our values of $-8.455(8)$ obtained with $\Delta\tau = 0.5$ GeV^{-1} and $-8.471(12)$ obtained with $\Delta\tau = 0.25$ GeV^{-1}.

There are also several other calculations of ^{4}He with Argonne v_{14} without V_{ijk}. Figure 10 shows the GFMC $E(\tau)$ for this case. Because there is no V_{ijk}, we multiplied the v'_{ij} in H' by 0.994 and included the isoscalar v'_C so that $\langle H - H' \rangle \sim 0$. The average, shown by the line and dotted error range, of the last few $E(\tau)$ is $-24.227(31)$ MeV. A calculation using the full v'_{ij}, without isoscalar v'_C, in H', gives $-24.230(31)$, even though in this case $\langle H - H' \rangle = 1.5$ MeV. These results are in excellent agreement with the older GFMC calculation of Ref. [41] (up-pointing triangle) which was made with a completely independent program that uses the short-time propagator of Eq. (4.12). They are also in excellent agreement with the correlated hyperspherical harmonic (CHH) value of -24.17 ± 0.05 MeV [42] shown by the open diamond. The error bar on the CHH value represents the expected truncation error in that calculation. However these results are below the Coulomb-corrected Faddeev-Yakubovsky value of -24.01 MeV [38], shown by the open
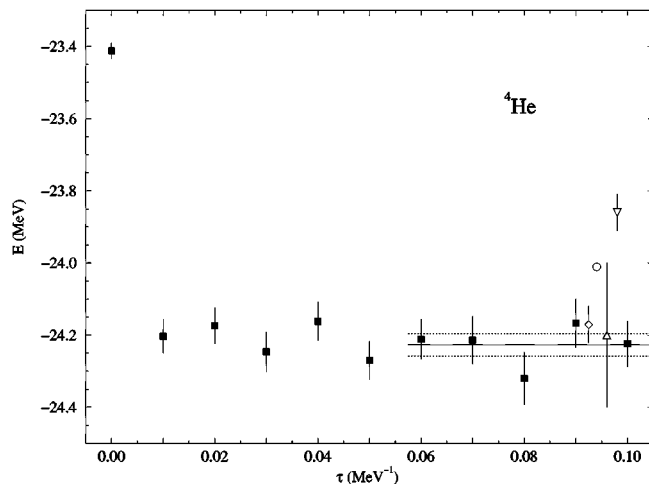
circle. The down-pointing triangle shows our best VMC upper bound for this case; it is $\sim 2\%$ higher than the exact E_0.

In the following sections we will give the calculated values of the average energy (E_{av}) for $\tau = 0.04$, 0.05, and 0.06 MeV^{-1} for various $A = 6$ and 7 states. These provide upper bounds to the eigenenergies of the nuclear Hamiltonian H used in this work. The studies of the accuracy of GFMC discussed above suggest that, assuming that the low-energy excitations in the Ψ_T have been successfully removed by diagonalizing the Hamiltonian matrix in the p-shell states, these E_{av} are at most ~ 0.3 MeV above the eigenenergies for $A = 6$ states. For the ^{6}Li ground state the additional binding obtained by single-energy extrapolations is only $\sim 0.13(15)$ MeV. This extrapolation was made using a factor 5 more samples than we have for the other states studied, thus no useful extrapolation estimates can be made for the other states. We also estimate that the perturbative treatment of $H - H'$ increases E_{av} by less than 0.1 MeV. As will be shown in the next section, the large τ behavior of $E(\tau)$ for all the $A = 6,7$ states is very similar. Thus we expect that the errors estimated for ^{6}Li are reasonable approximations to those for other nuclei. By scaling the above two errors according to $E(\tau = 0) - E_{\text{av}}$ and $\langle v_{ij} \rangle$ we estimate that the E_{av} for the $A = 7$ states is no more than ~ 0.5 MeV above the eigenenergies.

VII. ENERGY RESULTS

A. Ground states

The primary results of this paper are the GFMC energies, E_{av}, of the ten different ($J^\pi;T$) states in $A = 6,7$ nuclei shown in Table X and in Fig. 11, along with three isobaric analog states and the ground states of $A = 2-4$ nuclei. The present results for ^{6}He and ^{6}Li ground states and the (3^+;0) excited state in ^{6}Li are all slightly lower, but within error bars, of the τ-averaged results reported in Ref. [4]. The slight

FIG. 10. ^{4}He GFMC energy as a function of imaginary time for the Argonne v_{14} potential without V_{ijk}. Also shown are several previous calculations identified in the text.
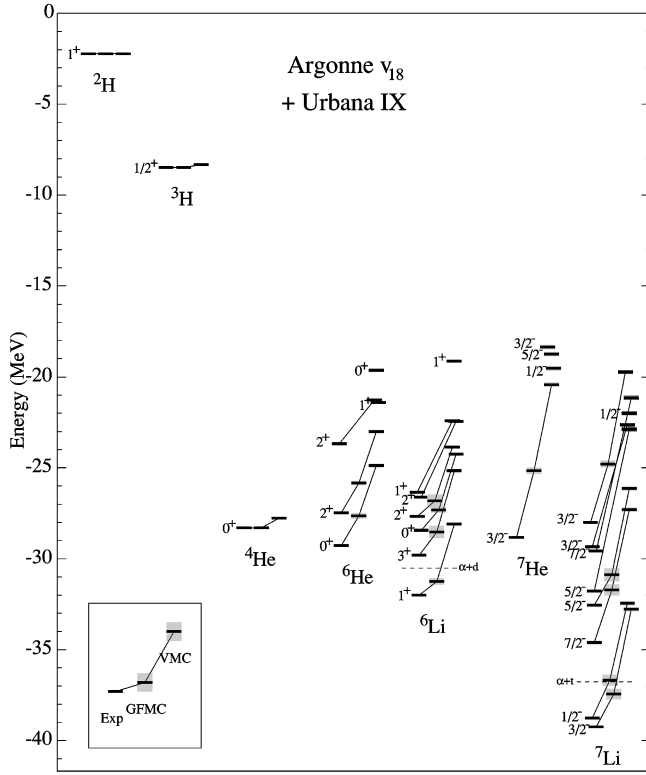
FIG. 11. Spectrum for $A=2-7$ nuclei from experiment, and in GFMC and VMC calculations.

improvement may be due to the improved Ψ_T, while we have obtained much better Monte Carlo statistics than previously, both by access to increased computer resources and by more efficient program implementation. The τ-extrapolated results of Ref. [4] were significantly below the present results, but also had a large uncertainty associated with the extrapolation; taking that uncertainty into account, the two calculations are consistent. In the particular case of the ^{6}Li

ground state, our earlier result of $-32.4(9)$ MeV was not inconsistent with the experimental binding of -31.99 MeV. However, from the various extrapolation tests discussed above, and the propagation to $\tau=0.1$ MeV^{-1}, we are now confident that the binding energy with the present Hamiltonian is not more than -31.6 MeV.

Table X also gives the VMC energies from the simple starting trial function, Ψ_T, and from the more sophisticated Ψ_V. In $A=3,4$ nuclei, Ψ_V picks up about 60% of the energy difference between Ψ_T and the final GFMC results. However, for the $A=6,7$ nuclei there is a much bigger gap between VMC calculations with Ψ_T and the GFMC energies, and the Ψ_V results recover only 20–25% of this energy difference. Clearly there is some important aspect to p-shell variational wave functions that is missing from the current *ansatz*.

The Argonne v_{18} + Urbana IX Hamiltonian was constructed to reproduce the experimental binding energies of ^{2}H, ^{3}H, and the equilibrium density of nuclear matter. From Table X and Fig. 11 we see that with this Hamiltonian all the $A=6$ and 7 states studied here are underbound. The discrepancy in ^{6}Li and ^{7}Li states is relatively small, $<2\%$ and $<5\%$ respectively, and the calculated ground states are stable against breakup into $\alpha+d$ and $\alpha+t$. On the other hand, the discrepancy in ^{6}He and ^{7}He states is larger, $\sim5\%$ and $\sim13\%$, respectively, and the calculated ^{6}He ground state is unstable against $\alpha+n+n$ breakup.

A breakdown of the GFMC energies into kinetic and potential contributions is given in Table XI. The kinetic and potential energies grow rapidly as the number of nucleons increases, but for a given nucleus, they decrease slightly as the excitation energy increases and the nucleus gets more diffuse. The V_{ijk} contribution remains small compared to v_{ij}, never exceeding 5%, but because of the large cancellation between K and v_{ij}, it is typically 25% of the total binding energy. The electromagnetic v_{ij}^γ is dominated by the Coulomb interaction between protons, $V_{C1}(pp)$, but about

TABLE XI. Kinetic and potential energy contributions to GFMC energies in MeV.

| $^AZ(J^\pi;T)$	K	v_{ij}	V_{ijk}	v_{ij}^γ	v_{ij}^π	$V_{ijk}^{2\pi}$
^{2}H$(1^+;0)$	19.81	-22.05	0.0	0.018	-21.28	0.0
^{3}H$(\frac{1}{2}^+;\frac{1}{2})$	50.0(8)	$-57.6(8)$	$-1.20(7)$	0.04	$-43.8(2)$	$-2.2(1)$
^{4}He$(0^+;0)$	112.1(8)	$-136.4(8)$	$-6.5(1)$	0.86(1)	$-99.4(2)$	$-11.8(1)$
^{6}He$(0^+;1)$	140.3(15)	$-165.9(15)$	$-7.2(2)$	0.87(1)	$-109.0(4)$	$-13.6(2)$
^{6}He$(2^+;1)$	131.9(14)	$-155.7(13)$	$-7.0(1)$	0.86(1)	$-106.2(5)$	$-13.1(2)$
^{6}Li$(1^+;0)$	150.8(10)	$-180.9(10)$	$-7.2(1)$	1.71(1)	$-128.9(5)$	$-13.7(3)$
^{6}Li$(3^+;0)$	146.7(29)	$-174.4(31)$	$-7.1(2)$	1.71(2)	$-119.9(5)$	$-13.9(4)$
^{6}Li$(0^+;1)$	135.1(16)	$-161.4(16)$	$-6.9(2)$	1.65(1)	$-108.5(4)$	$-12.9(2)$
^{6}Li$(2^+;0)$	139.6(32)	$-166.0(34)$	$-6.7(3)$	1.66(3)	$-119.2(5)$	$-12.4(4)$
^{6}Be$(0^+;1)$	134.8(16)	$-160.5(16)$	$-6.8(2)$	2.97(2)	$-108.0(4)$	$-12.8(2)$
^{7}He$(\frac{3}{2}^-;\frac{3}{2})$	146.0(17)	$-171.2(17)$	$-7.4(2)$	0.86(1)	$-109.9(6)$	$-14.1(2)$
^{7}Li$(\frac{3}{2}^-;\frac{1}{2})$	186.4(28)	$-222.6(30)$	$-8.9(2)$	1.78(2)	$-152.5(7)$	$-17.1(4)$
^{7}Li$(\frac{1}{2}^-;\frac{1}{2})$	183.0(32)	$-219.1(35)$	$-8.2(3)$	1.76(2)	$-151.5(7)$	$-16.1(4)$
^{7}Li$(\frac{7}{2}^-;\frac{1}{2})$	178.4(28)	$-209.6(30)$	$-8.5(3)$	1.78(2)	$-142.2(7)$	$-16.1(4)$
^{7}Li$(\frac{5}{2}^-;\frac{1}{2})$	169.1(31)	$-200.2(33)$	$-7.1(3)$	1.73(2)	$-143.2(7)$	$-14.2(4)$
^{7}Li$(\frac{3}{2}^-;\frac{3}{2})$	147.8(15)	$-173.8(15)$	$-7.2(2)$	1.68(1)	$-109.4(6)$	$-13.9(2)$
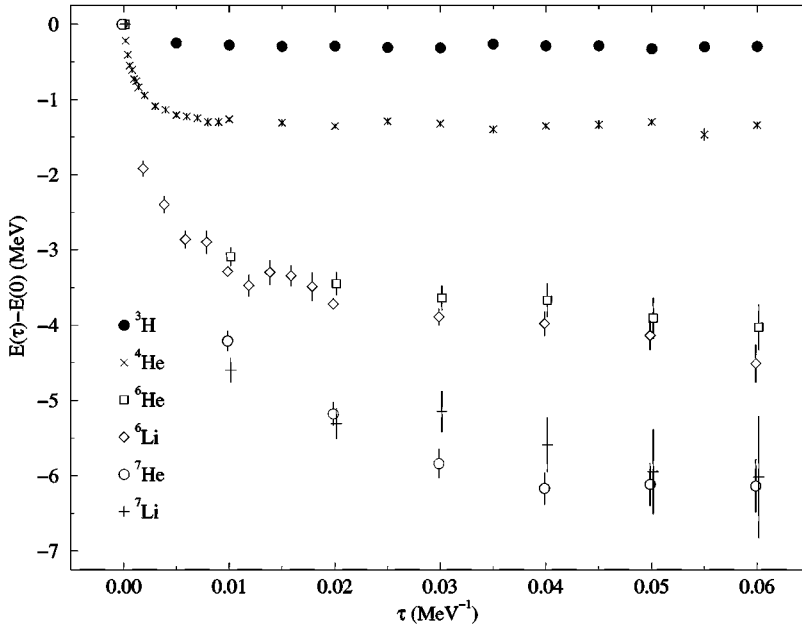
FIG. 12. $E(\tau)-E(\tau=0)$ for the ground states of $A=3$–7 nuclei.

17% (8%) of its total contribution comes from the magnetic moment and other terms in Eqs. (2.4)–(2.6) in He (Li) isotopes. The one-pion-exchange term of the potential dominates v_{ij}, providing $\sim$70% of the interaction energy, while the $V_{ijk}^{2\pi}$ is smaller than v_{ij}^{π} by one order of magnitude.

Figure 12 shows the $E(\tau)-E(\tau=0)$ from the GFMC calculations of ground states of nuclei with $3 \leq A \leq 7$. The GFMC correction to the VMC (Ψ_T) results has a strong A dependence but no significant $N-Z$ dependence. Figure 13 shows $[E(\tau)-E(0)]/|E_{av}-E(0)|$. The results for the two s-shell nuclei have the same dependence on τ, as do those for the four p-shell nuclei. However the p-shell $E(\tau)$ approach their asymptotic values less rapidly; a fit to the ^{6}Li $E(\tau)$ for $\tau < 0.03$ MeV^{-1} requires excitation energies of $\sim$ 700 and 90 MeV instead of the $\sim$ 1500 and 350 MeV used in the fit for ^{4}He shown in Fig. 4. This is another indication that there is a qualitatively new feature necessary for p-shell

nuclei which is missing from our trial wave functions; this feature does not seem to depend on the $N-Z$, J^{π}, or T of the nucleus.

B. Excited states

A second result of the present paper is the prediction of an additional dozen higher excited states obtained in the VMC calculations as shown in Table XII, and in Fig. 14. We have calculated VMC and GFMC excitation energies for eight states, and they agree with each other within error bars in all cases. Therefore, we may expect that the VMC excitation energies for the other states shown are close to the correct results for this Hamiltonian. Most of these higher states are obtained by the diagonalizations within correlated p-shell states discussed in Sec. III.

In Fig. 11 we see that the difference between the calculated and experimental energies increases as A and $|N-Z|$
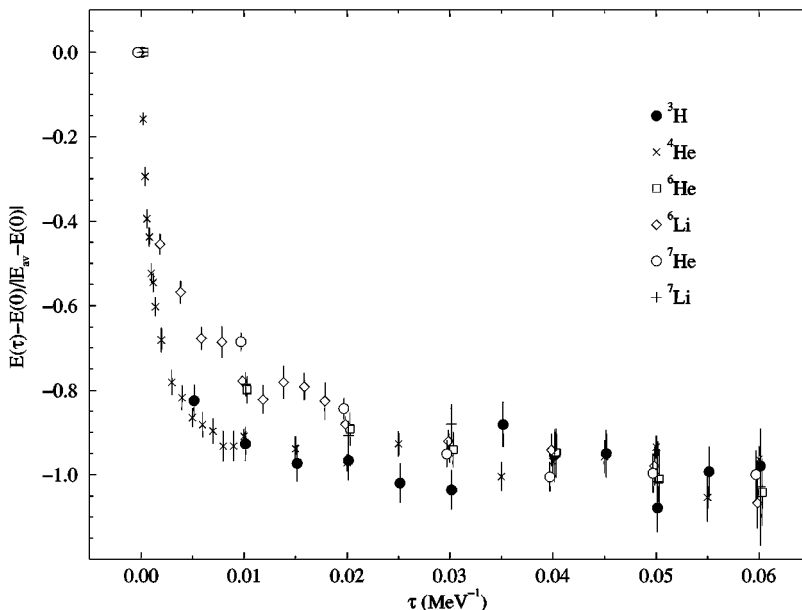

FIG. 13. $E(\tau)-E(0)/|E_{av}-E(0)|$ for the ground states of $A=3$–7 nuclei.

TABLE XII. Experimental, VMC, and GFMC excitation energies (adjusted to their respective ground states) in MeV.

$^AZ(J^\pi;T)$	Expt.	VMC	GFMC
^{6}He$(2^+;1)$	1.80	1.86(10)	1.80(18)
^{6}He$(2^+;1)$	5.6	3.61(10)	
^{6}He$(1^+;1)$		3.46(10)	
^{6}He$(0^+;1)$		5.24(11)	
^{6}Li$(3^+;0)$	2.19	2.93(10)	2.72(36)
^{6}Li$(0^+;1)$	3.56	3.84(10)	3.94(23)
^{6}Li$(2^+;0)$	4.31	4.23(11)	4.43(39)
^{6}Li$(2^+;1)$	5.37	5.64(10)	
^{6}Li$(1^+;0)$	5.65	5.68(11)	
^{6}Li$(1^+;0)$		8.96(11)	
^{7}He$(\frac{1}{2}^-;\frac{3}{2})$		0.90(16)	
^{7}He$(\frac{5}{2}^-;\frac{3}{2})$		1.69(16)	
^{7}He$(\frac{3}{2}^-;\frac{3}{2})$		2.08(16)	
^{7}Li$(\frac{1}{2}^-;\frac{1}{2})$	0.48	0.33(16)	0.76(41)
^{7}Li$(\frac{7}{2}^-;\frac{1}{2})$	4.63	5.48(16)	5.72(41)
^{7}Li$(\frac{5}{2}^-;\frac{1}{2})$	6.68	6.64(16)	6.56(45)
^{7}Li$(\frac{5}{2}^-;\frac{1}{2})$	7.46	9.90(16)	
^{7}Li$(\frac{7}{2}^-;\frac{1}{2})$	9.67	11.63(16)	
^{7}Li$(\frac{3}{2}^-;\frac{1}{2})$	9.90	10.14(16)	
^{7}Li$(\frac{1}{2}^-;\frac{1}{2})$		10.79(16)	
^{7}Li$(\frac{3}{2}^-;\frac{3}{2})$	11.24	13.05(16)	12.65(33)

FIG. 14. Excitation spectrum for $A=6,7$ nuclei from experiment, and in GFMC and VMC calculations.

increase. However, as seen in Fig. 14, the excitation spectra are in good overall agreement with experiment. The states generally occur in the correct order, and with reasonable energies. The agreement with the ^{6}Li and low-lying ^{7}Li spectra is very good. In particular, the first excited $(1^+;0)$ state in ^{6}Li, and the first excited $(\frac{3}{2}^-;\frac{1}{2})$ state in ^{7}Li, i.e., the first excited states with quantum numbers identical to the ground states, are very close to the observed excitations. In the case of ^{6}He and ^{7}He, we predict a number of states that have not been observed experimentally, but which could be searched for. A first observation of the second $(2^+;1)$ state in ^{6}He was recently reported [19]; the experimenters tried to fit their data with single states of different $(J^\pi;T)$ but did not get a very good fit for any one value. Our results suggest there are several states close together in this region, which could improve the chances of fitting the data satisfactorily. The states in ^{7}He might also be amenable to experimental measurement with the new radioactive beam facilities that are now coming on line.

C. Isobaric analog states

Energy differences of isobaric analog states are sensitive probes of the charge-independence-breaking parts of the Hamiltonian. To study these it is useful to express the energies in an isobaric multiplet, characterized by A and T, in terms of the isospin multipole operators of order n:
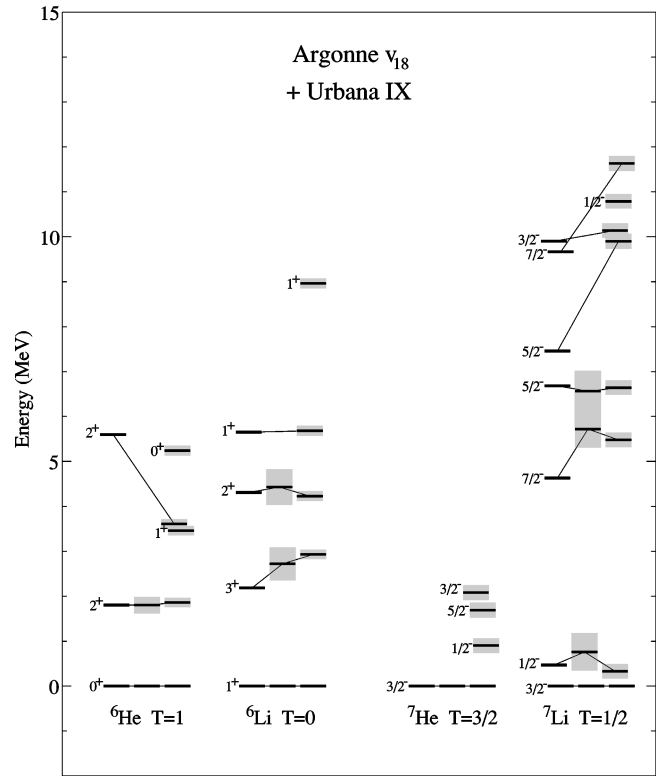
$$E_{A,T}(T_z)=\sum_{n\leqslant 2T} a_{A,T}^{(n)}Q_n(T,T_z). \tag{7.1}$$

The $Q_n(T,T_z)$ are orthogonal functions for projecting out isovector, isotensor, and higher-order terms [43]; the first terms are $Q_0=1$, $Q_1=T_z$, and $Q_2=\frac{1}{2}(3T_z^2-T^2)$. The coefficients $a^{(n)}$ are then obtained from

$$a_{A,T}^{(n)}=\sum_{T_z} Q_n(T,T_z)E_{A,T}(T_z)/\sum_{T_z} Q_n^2(T,T_z). \tag{7.2}$$

In first-order perturbation theory, the electromagnetic interaction contributes to the $a^{(n)}$ for $n=1$ and 2, the nuclear CSB potential and kinetic energy contribute to $n=1$, and the nuclear CD potential contributes to $n=2$. The $a^{(n)}$ for higher n are zero in first order with our Hamiltonian, and there is little experimental evidence for $n\geqslant 3$ terms in nuclei [44]. We have made VMC calculations of the $a^{(1,2)}$ in first order by using a CI wave function of good isospin, T, and simply varying T_z to compute the $E_{A,T}(T_z)$. Table XIII contains results for the $T=\frac{1}{2}$ isovector $(n=1)$ coefficients in $A=3$ and $A=7$, the $T=1$ isovector and isotensor $(n=2)$ coefficients in $A=6$, and the $T=\frac{3}{2}$ isovector and isotensor coefficients in $A=7$. The energy differences are broken down into v^γ, v^{CD}, v^{CSB}, and K^{CSB} contributions, with the pp Coulomb, $[v_{C1}(pp)]$, other Coulomb (v_{CR}), and magnetic moment (v_{MM}) components of v^γ also given.

The CIB parts of the Hamiltonian induce CD changes in the nuclear wave function, leading to higher-order perturbative corrections to the splittings of the isospin multiplets. We have estimated some of these changes in VMC by repeating

TABLE XIII. Breakdown of VMC isovector and isotensor energy coefficients $a_{A,T}^{(n)}$ (in MeV) obtained with CI wave functions. Total coefficients are given for VMC with CI and CD wave functions, and for GFMC CD wave functions in $A=6$ nuclei.

A,T,n	$3,\frac{1}{2},1$	$6,1,1$	$6,1,2$	$7,\frac{1}{2},1$	$7,\frac{3}{2},1$	$7,\frac{3}{2},2$
$\langle v^\gamma \rangle$	0.680(1)	1.048(2)	0.186(1)	1.501(3)	1.109(4)	0.119(1)
$[\langle v_{C1}(pp) \rangle]$	[0.651]	[1.030]	[0.167]	[1.458]	[1.099]	[0.114]
$[\langle v_{CR \ldots} \rangle]$	[0.011]	[0.014]	[0.001]	[0.021]	[0.012]	[0.001]
$[\langle v_{MM} \rangle]$	[0.018]	[0.004]	[0.018]	[0.023]	[−0.002]	[0.004]
$\langle K^{\text{CSB}} \rangle$	0.014	0.014	0	0.025	0.011	0
$\langle v^{\text{CSB}} \rangle$	0.066	0.035(1)	0	0.080(1)	0.021(2)	0
$\langle v^{\text{CD}} \rangle$	0	0	0.101(12)	0	0	0.020(4)
$a_{A,T}^{(n)}$ (VMC: CI)	0.760(1)	1.097(3)	0.287(12)	1.605(4)	1.141(5)	0.139(4)
$a_{A,T}^{(n)}$ (VMC: CD)	0.760(1)	1.082(3)	0.277(12)	1.597(4)	1.125(5)	0.132(4)
$a_{A,T}^{(n)}$ (GFMC: CD)	0.756(1)	1.120(9)	0.256(11)			
$a_{A,T}^{(n)}$ (Expt.)	0.764	1.173	0.223	1.644	1.373	0.175

the calculations using wave functions that have a varying Coulomb term, $V_{\alpha N}^C$ of Eq. (3.20), added to the single-particle potential well that is used to generate the $\phi_p^{LS}(R_{\alpha k})$ components of Ψ_V. This results in a slightly more diffuse wave function as Z increases, and slightly smaller energy coefficients than those obtained with CI wave functions. In the GFMC calculations, the isoscalar Coulomb term, v_C', provides an additional source of CIB through the propagating Hamiltonian of Eq. (2.17), which depends on T_z. However, within the limited propagation time of $\tau = 0.06\,\text{MeV}^{-1}$, the main effect of using GFMC wave functions seems to be the slightly sharper two-body densities (discussed below) around 1 fm, and consequent changes in the CIB potential expectation values. All our GFMC calculations have been made with CD wave functions, but a complete set of isobaric analog states was calculated only for $A=6$, results for which are shown on the penultimate line of Table XIII. There may also be higher-order contributions to the isomultiplet splittings from changes to the CI expectation values, but we have no reliable way of extracting these from under the sizeable Monte Carlo errors.

The results tabulated in Table XIII indicate that the present Hamiltonian underestimates the observed isovector coefficients and gives mixed results for the isotensors. It should be remembered, however, that while v^{CD} is well determined in the $\ell=0$ partial wave by the NN scattering data, it is much less well known in $\ell=1$ and higher partial waves, while the only experimental input for v^{CSB} is the nn-pp scattering length difference, which has a 20% experimental uncertainty. The $A=3$ case would be corrected by a $\sim 10\%$ increase in v^{CSB}, but this would not explain much of the discrepancy in the larger nuclei. The significant underbinding of the $A=6,7$ nuclei with the present Hamiltonian may mean that our wave functions for these nuclei are more diffuse than they should be. By far the worst discrepancy is for the $A,T=7,\frac{3}{2}$ case, where the underbinding of the ground states is also the largest. If the Hamiltonian were altered, e.g., by increasing the net attraction from the three-nucleon interaction, to obtain the correct binding, the contribution of the CIB forces to the isovector coefficients should be increased, both in the dominant pp Coulomb term, and the short-range v^{CSB}. It is more difficult to predict the effect of such changes on the isotensor energy coefficients.

TABLE XIV. VMC values for proton rms radii (in fm), for quadrupole moments (in fm^2), and magnetic moments (in μ_N) all in impulse approximation.

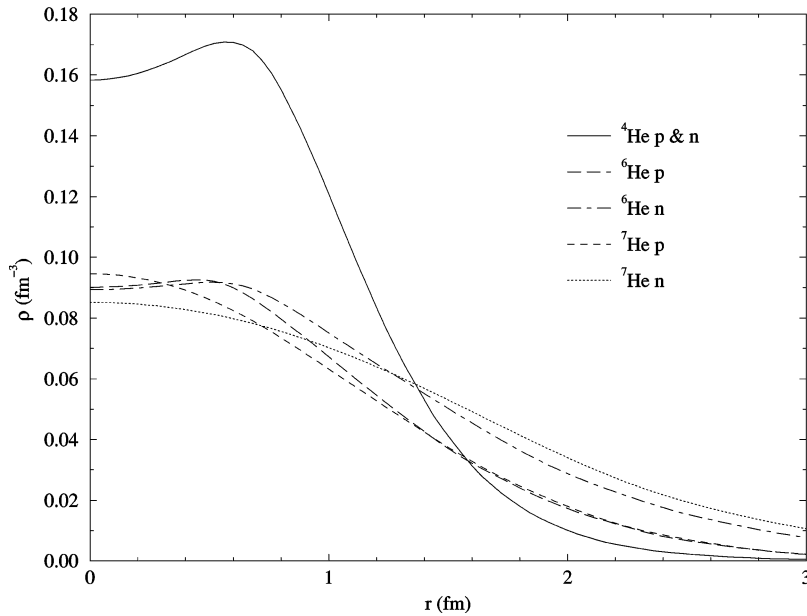|	$\langle r_p^2 \rangle^{1/2}$		μ		Q	
	VMC	Expt.	VMC	Expt.	VMC	Expt.
$^2\text{H}(1^+;0)$	1.967	1.953	0.847	0.857	0.270	0.286
$^3\text{H}(\frac{1}{2}^+;\frac{1}{2})$	1.59(1)	1.60	2.582(1)	2.979		
$^3\text{He}(\frac{1}{2}^+;\frac{1}{2})$	1.74(1)	1.77	−1.770(1)	−2.128		
$^4\text{He}(0^+;0)$	1.47(1)	1.47				
$^6\text{He}(0^+;1)$	1.95(1)					
$^6\text{Li}(1^+;0)$	2.46(2)	2.43	0.828(1)	0.822	−0.33(18)	−0.083
$^6\text{Be}(0^+;1)$	2.96(4)					
$^7\text{Li}(\frac{3}{2}^-;\frac{1}{2})$	2.26(1)	2.27	2.924(2)	3.256	−3.31(29)	−4.06
$^7\text{Be}(\frac{3}{2}^-;\frac{1}{2})$	2.42(1)		−1.110(2)		−5.64(45)	

FIG. 15. The neutron and proton densities in ^{4}He, ^{6}He, and ^{7}He.

VIII. ONE- AND TWO-NUCLEON DISTRIBUTIONS

The one- and two-nucleon distributions of light p-shell nuclei are interesting in a variety of experimental settings. For example, the ^{6}He nucleus has been a popular candidate for study as a ''halo'' nucleus whose last two neutrons are weakly bound. In addition, the polarization densities of ^{6}Li and ^{7}Li are important because of possible applications in polarized targets. In order to extract information on the spin-dependent nucleon properties from experiments on such targets one must, at a minimum, understand the nucleon polarization in the polarized nucleus. In this section we provide our results for a variety of nucleon distributions, including spin-polarized and averaged single-nucleon densities, spin-dependent and spin-independent two-body densities, the proton-proton distributions, and the rms radii, magnetic moments, and quadrupole moments.

As was discussed in Sec. VI, we do not propagate to large enough imaginary time to allow the GFMC to significantly

modify the rms radius of the p-shell nuclei. Thus they are determined almost entirely by the input trial wave function, which is constrained to be near the experimental value wherever known. However GFMC does make significant changes to densities at small r. A number of the one-body densities are increased near the origin, as are the peaks of many of the two-body densities.

The proton rms radii and static electromagnetic properties are given in Table XIV. These are calculated from Ψ_V using impulse approximation. In general, we know that there are significant corrections to the electromagnetic moments from two-body charge and current contributions [45,46]. For the magnetic moments, these corrections are only $\sim$ 1–2% in isoscalar nuclei like ^{2}H, but are $\sim$ 15–20% in the isovector $T=\frac{1}{2}$ nuclei ^{3}H and ^{3}He. Therefore it is not surprising that we see very little discrepancy for the magnetic moment in ^{6}Li, but a sizeable error for ^{7}Li; presumably, a calculation including meson-exchange contributions would come much
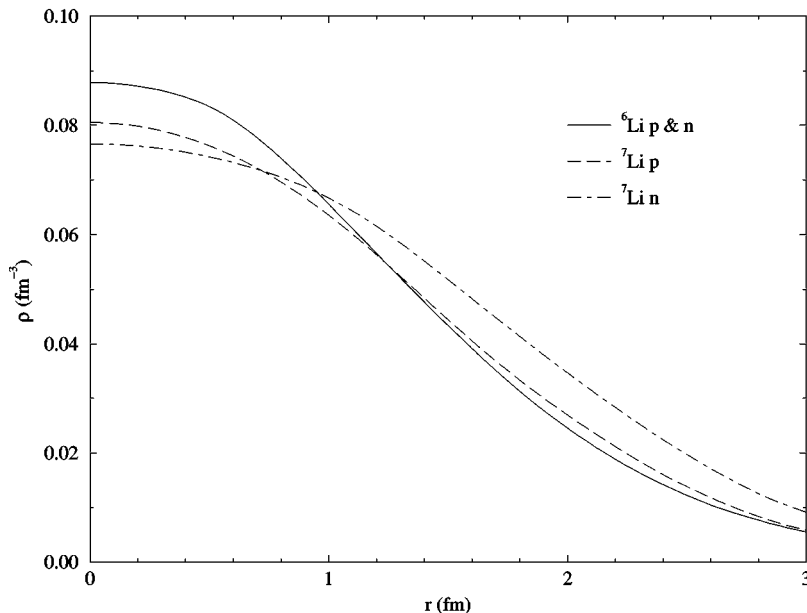

FIG. 16. The neutron and proton densities in ^{6}Li and ^{7}Li.
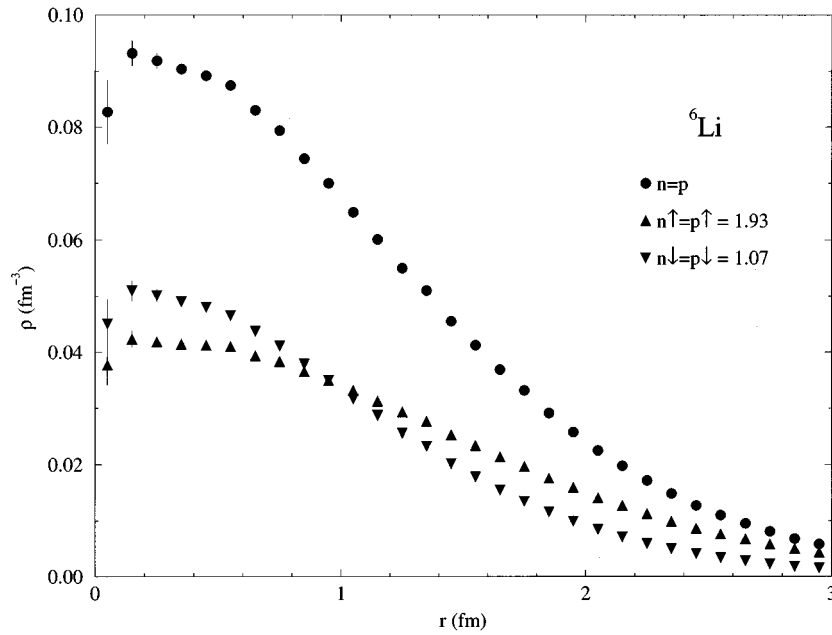
FIG. 17. The spin-up and spin-down neutron and proton densities in ^{6}Li.

closer to the experimental values in the latter case. The quadrupole moment is a more difficult problem, particularly in ^{6}Li, where there is a delicate cancellation between the contributions from the deuteron quadrupole moment and the D-wave part of the α-d relative wave function. Many cluster models for ^{6}Li fail to obtain the observed negative sign; we have trouble getting an accurate measure of the magnitude, for reasons discussed above. In the case of ^{7}Li, where there is no such delicate cancellation, the value is only $\sim$ 15–20% too low in magnitude. Again, some of this discrepancy might be made up by meson-exchange corrections.

In Fig. 15, we present the neutron and proton densities for the helium isotopes, calculated with GFMC. Previously we have found that the ^{4}He charge form factor is in good agreement with experimental data in realistic calculations [46], and hence this distribution should be quite accurate. As more neutrons are added, the tails of the distributions broaden con-

siderably because of the relatively weak binding of the p-shell neutrons. In addition, the central neutron and proton densities decrease rather dramatically. This effect does not necessarily require any changes to the α-particle core, but can be understood at least partially from the fact that the α particle no longer sits at the center of mass of the entire system. The motion relative to the center of mass spreads out the mass distribution relative to that of ^{4}He.

We also find that the small depression obtained in the central density of ^{4}He gradually disappears as more nucleons are added. While the depression is clear in the α particle, it is nearly within our statistical errors in ^{6}He and seems to have disappeared completely in ^{7}He. This can again be understood by taking into account the fluctuations in the center of mass of the core nucleons about the center of mass of the entire system. Figure 16 shows the GFMC neutron and proton densities for the lithium isotopes. These densities are
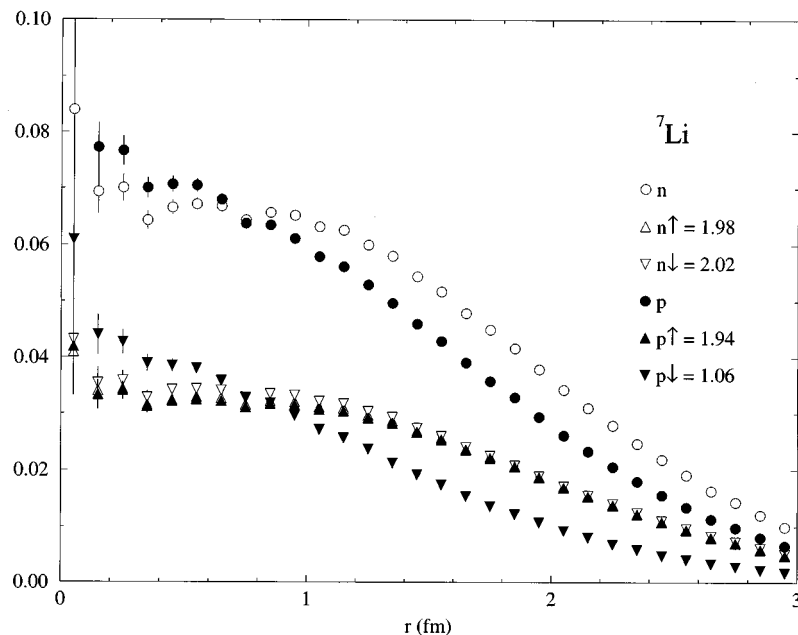

FIG. 18. The spin-up and spin-down neutron and proton densities in ^{7}Li.

very smooth functions of the distance from the center of mass.

The polarization densities for ^{6}Li and ^{7}Li, computed with VMC are presented in Figs. 17 and 18, respectively. The spin-up proton density distribution is defined by

$$\rho_{p\uparrow}(r) = \frac{1}{4\pi r^2} \left\langle \Psi(J,M_J=J) \left| \sum_i \frac{1+\sigma_z(i)}{2} \frac{1+\tau_z(i)}{2} \right. \right.$$

$$\left. \left. \times \delta(r-|\mathbf{r}_i-\mathbf{R}_{cm}|) \right| \Psi(J,M_J=J) \right\rangle, \qquad (8.1)$$

with similar definitions for spin-down protons, spin-up neutrons, etc. The integral of these distributions is the total number of spin-up (down) protons (neutrons) in a fully polarized state. The integrated quantities can be important in high-energy experiments designed to probe the spin-dependence of the neutron or proton structure functions, while their radial dependence may be partially accessible in experiments at lower energies. Experimentalists are considering using dense, solid polarized ^{6}LiD targets, as an alternative to the deuterated ammonia targets currently being used to probe neutron properties.

Polarization densities have been studied previously in cluster models, with a fixed (unpolarized) α core plus interacting valence nucleons. Our calculations include the possibility of the spins in the the core α particle being polarized by the valence nucleon's spin and orbital angular momentum, and hence it is interesting to examine the results for both the distributions and the integrated quantities.

In the spin projection $M=1$ state of the deuteron, the polarization of the neutron differs from unity because the tensor interaction induces a D state in the wave function. Integrating $\rho_{n\uparrow}(r)$ over r yields a probability for up-spin neutrons of

$$P(n\uparrow) = P_S + \tfrac{1}{4} P_D = 1 - \tfrac{3}{4} P_D, \qquad (8.2)$$

where P_S and P_D are the S- and D-wave probabilities of the deuteron. In the simplest two-body (α plus deuteron) model
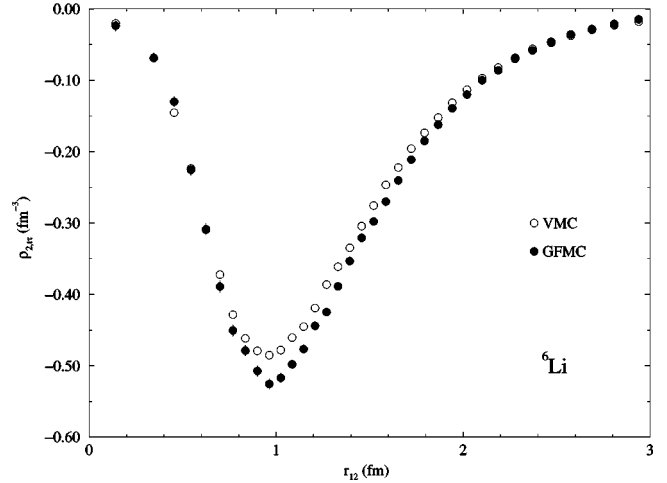

FIG. 19. The two-nucleon $S_{ij}\tau_i\cdot\tau_j$ density of ^{6}Li computed from Ψ_T and by GFMC.

of ^{6}Li, the polarization of the neutrons is determined by the D-state probability in the deuteron and the D-state probability in the $\alpha-d$ wave function. In three-body models, recent calculations [47] have found that the valence neutron had $P(n\uparrow)=0.93(1)$. Since in such a model the two core neutrons are unpolarized, this corresponds to a total projection $P(n\uparrow)$ of 1.93, or a polarization of 29%.

As expected, the up spins dominate the down spins in the $M=1$ state of ^{6}Li at large distances from the center of mass. At very large separations, the ratio will be determined solely by the asymptotic D/S state normalization of the α-deuteron wave function and the D-state probability in the deuteron. At small r, we find that the spin-down density exceeds the spin-up density, presumably because the spins of the outer nucleons prefer to try to pair with the core nucleons to a spin-zero state. Even though we find this effect to be significant, the integrated spin densities agree reasonably well with the cluster model calculations. The integrated neutron densities in ^{6}Li are found to be 1.93 for spin up and 1.07 for spin down, respectively, yielding the same net polarization of 29%.

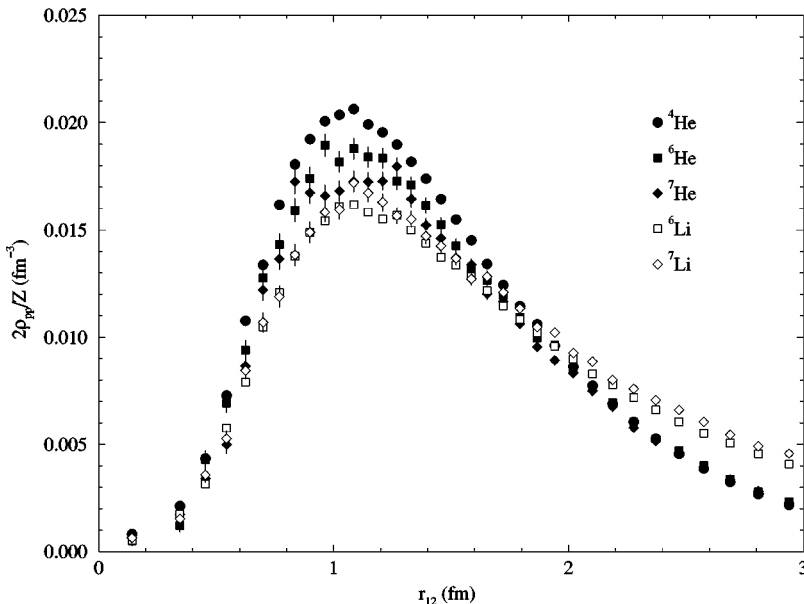FIG. 20. The proton-proton densities in ^{4}He, ^{6}He, ^{7}He, ^{6}Li, and ^{7}Li nuclei.

The $P(p\uparrow)$ in ^{7}Li is found to be 1.94 instead of 2 as predicted by the independent-particle shell model. The neutrons carry about half this remaining spin, as the spin-up and spin-down neutron integrated densities are 1.98 and 2.02.

We have also computed a variety of two-nucleon distribution functions. These are defined by

$$\rho_{2,p}(r) = \frac{1}{4\pi r^2}\left\langle \Psi \left| \sum_{i<j} O_{ij}^p \delta(r - |\mathbf{r}_i - \mathbf{r}_j|) \right| \Psi \right\rangle, \quad (8.3)$$

where the operators O_{ij}^k are given in Eq. (3.9). While typically these two-body correlations cannot be directly measured, they provide the expectation values of two-body operators and can be important ingredients in interpreting the results of experiments. Transition matrix elements of this type are needed for extracting the effective weak πNN coupling constant in parity-violating experiments. Figure 19 shows VMC and GFMC calculations of the $S_{ij}\tau_i\cdot\tau_j$ NN pair distribution function. This correlation is strongly dominated by pion exchange, and is responsible for the toroidal shapes which characterize the coupling of spin to space in the nucleus [48]. We see that the structure is somewhat enhanced by the GFMC.

Finally, we present the proton-proton distributions (scaled to have normalization integrals of $Z-1$) for ^{4}He, ^{6}He, ^{7}He, ^{6}Li, and ^{7}Li in Fig. 20. These distributions are directly related to the Coulomb sum measured in inclusive longitudinal electron scattering; such measurements in ^{3}He have been used [49] to put constraints on the $\rho_{pp}(r_{ij})$, and realistic calculations agree with the experimental results [50]. The behavior of $\rho_{pp}(r)$ at short distances is largely determined by the repulsive core of the NN potential and is nearly independent of the nucleus, but at larger distances it is determined by the size of the nucleus.

We show results for ρ_{pp} in ^{6}He and ^{7}He in order to directly compare the α particle proton-proton distribution to that in the α-particle cores of ^{6}He and ^{7}He. Unlike the one-body densities, these distributions are not sensitive to center-of-mass effects. We find that the proton-proton distribution spreads out slightly with neutron number in the helium isotopes, with an increase of the pair rms radius of approximately 4% in going from ^{4}He to ^{6}He, and 7% to ^{7}He. While this could be interpreted as a swelling of the α core, it might also be due to the charge-exchange ($\tau_i\cdot\tau_j$) correlations which can transfer the charge from the core to the valence nucleons. Since these correlations are rather long-ranged, they can have a significant effect on the proton-proton distribution.

Finally, we mention that calculations of the electromagnetic ground-state and transition form factors are underway. Complete results for these quantities, including exchange current effects, will appear in a separate paper.

IX. CONCLUSIONS

Quantum Monte Carlo (QMC) methods are now a powerful tool for the study of light p-shell nuclei. At present, we can write plausible variational wave functions with the proper quantum numbers for the given state of interest, but they do not give sufficient binding to provide stability against breakup into subclusters. However, the GFMC method rapidly damps out the small amount of highly excited states contained in the VMC wave functions, producing ground states that are stable in the case of ^{6}Li and ^{7}Li. The current major limitation is the small value of τ that can be reached in most calculations. This makes it important that the starting VMC wave functions have a proper mix of the appropriate spatial symmetries, and negligible contamination from low-energy excited states.

The energies obtained for the ground and low-lying excited states are close to, but somewhat above, the experimental numbers. We believe the discrepancy is probably the fault of the Hamiltonian, most likely the phenomenological short-range part of the three-nucleon interaction, rather than a shortcoming of the calculation. We note that the difference between experimental and theoretical energies is much less that $\langle V_{ijk}\rangle$, and might be rectified by an improved three-nucleon potential. Despite the discrepancies in the ground-state energies, the excitation spectra are reproduced very well. We believe this is a demonstration that the shell structure of light nuclei can be obtained directly from bare two-nucleon interactions that fit NN scattering data.

The QMC methods developed here can be extended to eight-body nuclei with the present generation of computers. We already have calculations in progress for the ground and low-lying excited states of $A=8$ nuclei. The next major task will be to refine our model for the three-nucleon interaction, perhaps including those relativistic corrections which first appear at the three-nucleon level [14,15], with the intention of fitting the energies of $A=3$–8 nuclear states with 1% accuracy. Now that accurate QMC calculations of these states are possible, there are a host of interesting problems that become accessible, including the response of ^{6}Li and ^{7}Li to electron scattering, and many low-energy electroweak capture reactions of astrophysical interest, such as ^{4}He(d,γ)^{6}Li and ^{7}Be(p,γ)^{8}B. There also remains the problem of adapting the GFMC methods here to the study of larger systems, perhaps through methods similar to the cluster expansion used in VMC calculations of ^{16}O [51].

[1] S. Cohen and D. Kurath, Nucl. Phys. **73**, 1 (1965); Nucl. Phys. **A101**, 1 (1967).

[2] D. C. Zheng, B. R. Barrett, J. P. Vary, W. C. Haxton, and C.-L. Song, Phys. Rev. C **52**, 2488 (1995).

[3] V. I. Kukulin, V. N. Pomerantsev, Kh. D. Razikov, V. T. Voronchev, and G. G. Ryzhikh, Nucl. Phys. **A586**, 151 (1995).

[4] B. S. Pudliner, V. R. Pandharipande, J. Carlson, and R. B. Wiringa, Phys. Rev. Lett. **74**, 4396 (1995).

[5] R. B. Wiringa, V. G. J. Stoks, and R. Schiavilla, Phys. Rev. C **51**, 38 (1995).

[6] J. Carlson, V. R. Pandharipande, and R. B. Wiringa, Nucl. Phys. **A401**, 59 (1983).

[7] A. Arriaga, V. R. Pandharipande, and R. B. Wiringa, Phys. Rev. C **52**, 2362 (1995).

[8] J. Carlson, Phys. Rev. C **38**, 1879 (1988).

[9] J. R. Bergervoet, P. C. van Campen, R. A. M. Klomp, J.-L. de Kok, T. A. Rijken, V. G. J. Stoks, and J. J. de Swart, Phys. Rev. C **41**, 1435 (1990).

[10] V. G. J. Stoks, R. A. M. Klomp, M. C. M. Rentmeester, and J. J. de Swart, Phys. Rev. C **48**, 792 (1993).

[11] J. Fujita and H. Miyazawa, Prog. Theor. Phys. **17**, 360 (1957).

[12] S. A. Coon, M. T. Peña, and D. O. Riska, Phys. Rev. C **52**, 2925 (1995).

[13] G. E. Brown, W. Weise, G. Baym, and J. Speth, Comments Nucl. Part. Phys. **17**, 39 (1987).

[14] J. L. Forest, V. R. Pandharipande, and J. L. Friar, Phys. Rev. C **52**, 568 (1995).

[15] J. L. Forest, V. R. Pandharipande, J. Carlson, and R. Schiavilla, Phys. Rev. C **52**, 576 (1995).

[16] R. B. Wiringa, Rev. Mod. Phys. **65**, 231 (1993).

[17] R. B. Wiringa, Phys. Rev. C **43**, 1585 (1991).

[18] F. Ajzenberg-Selove, Nucl. Phys. **A490**, 1 (1988).

[19] J. Jänecke *et al.*, Phys. Rev. C **54**, 1070 (1996).

[20] A. Bohr and B. R. Mottelson, *Nuclear Structure Volume I* (Benjamin, New York, 1969).

[21] J. A. Carlson and R. B. Wiringa, in *Computational Nuclear Physics 1*, edited by K. Langanke, J. A. Maruhn, and S. E. Koonin (Springer-Verlag, Berlin, 1991).

[22] B. S. Pudliner, Ph.D. thesis, University of Illinois, 1996.

[23] R. Schiavilla, V. R. Pandharipande, and A. Fabrocini, Phys. Rev. C **40**, 1484 (1989).

[24] M. H. Kalos, J. Comput. Phys. **2**, 257 (1967).

[25] D. M. Ceperley and M. H. Kalos, in *Monte Carlo Methods in Statistical Physics*, edited by K. Binder (Springer-Verlag, Heidelberg, 1979).

[26] J. Carlson, Phys. Rev. C **36**, 2026 (1987).

[27] D. M. Ceperley, Rev. Mod. Phys. **67**, 279 (1995).

[28] K. E. Schmidt and M. A. Lee, Phys. Rev. E **51**, 5495 (1995).

[29] J. Carlson, Nucl. Phys. **A508**, 141c (1990).

[30] V. R. Pandharipande, J. G. Zabolitzky, S. C. Pieper, R. B. Wiringa, and U. Helmbrecht, Phys. Rev. Lett. **50**, 1676 (1983).

[31] S. C. Pieper, R. B. Wiringa, and V. R. Pandharipande, Phys. Rev. B **32**, 3341 (1985).

[32] K. E. Schmidt and M. H. Kalos, in *Applications of the Monte Carlo Method in Statistical Physics*, edited by K. Binder (Springer-Verlag, Heidelberg, 1984).

[33] E. Y. Loh, Jr., J. E. Gubernatis, R. T. Scalettar, S. R. White, D. J. Scalapino, and R. L. Sugar, Phys. Rev. B **41**, 9301 (1990).

[34] J. Carlson, J. L. Friar, and G. L. Payne, Phys. Rev. C **37**, 420 (1988).

[35] B. L. Hammond, W. A. Lester, Jr., and P. J. Reynolds, *Monte Carlo Methods in ab initio Quantum Chemistry* (World Scientific, Singapore, 1994).

[36] H. Kamada and W. Glöckle (private communication).

[37] C. R. Chen, G. L. Payne, J. L. Friar, and B. F. Gibson, Phys. Rev. C **31**, 2266 (1985).

[38] W. Glöckle, H. Kamada, H. Witala, D. Hüber, J. Golak, K. Miyagawa, and S. Ishikawa, in *Few Body Systems Suppl. 8*, edited by R. Guardiola (Springer-Verlag, Wien, 1995), p. 9.

[39] A. Kievsky, M. Viviani, and S. Rosati, Nucl. Phys. **A577**, 511 (1994).

[40] M. Viviani (private communication).

[41] J. Carlson and R. Schiavilla, in *Few Body Systems Suppl. 7*, edited by B. L. G. Bakker and R. van Dantzig (Springer-Verlag, Wien, 1994), p. 349.

[42] M. Viviani, A. Kievsky, and S. Rosati (unpublished).

[43] M. Peshkin, Phys. Rev. **121**, 636 (1960).

[44] W. Benenson and E. Kashy, Rev. Mod. Phys. **51**, 527 (1979).

[45] R. Schiavilla, V. R. Pandharipande, and D. O. Riska, Phys. Rev. C **40**, 2294 (1989).

[46] R. Schiavilla, V. R. Pandharipande, and D. O. Riska, Phys. Rev. C **41**, 309 (1990).

[47] N. W. Schellingerhout, L. P. Kok, S. A. Coon, and R. M. Adam, Phys. Rev. C **48**, 2714 (1993); **52**, 439 (1995).

[48] J. L. Forest, V. R. Pandharipande, S. C. Pieper, R. B. Wiringa, R. Schiavilla, and A. Arriaga, Phys. Rev. C **54**, 646 (1996).

[49] D. H. Beck, Phys. Rev. Lett. **64**, 268 (1990).

[50] R. Schiavilla, R. B. Wiringa, and J. Carlson, Phys. Rev. Lett. **70**, 3856 (1993).

[51] S. C. Pieper, R. B. Wiringa, and V. R. Pandharipande, Phys. Rev. C **46**, 1741 (1992).